The Description and Validation of a Computationally-Efficient CH_4-CO-OH (ECCOH) Module for 3D Model Applications

Elshorbany, Yasin F.[1,2*], Duncan, Bryan N.[1], Strode, Sarah A.[1,3], Wang, James S.[1,3], Kouatchou, Jules[1,4]

[1]NASA Goddard Space Flight Center, Greenbelt, Maryland, USA.

[2]Earth System Science Interdisciplinary Center, University of Maryland, College Park, Maryland, USA.

[3]Universities Space Research Association, Columbia, Maryland, USA

[4] Science Systems and Applications Inc., Lanham, Maryland, USA

*Correspondence to: Y. F. Elshorbany (yasin.f.elshorbany@nasa.gov)

Abstract:

We present the Efficient CH_4-CO-OH Module (ECCOH) that allows for the simulation of the methane, carbon monoxide and hydroxyl radical (CH_4-CO-OH cycle, within a chemistry climate model, carbon cycle model, or earth system model. The computational efficiency of the module allows many multi-decadal, sensitivity simulations of the CH_4-CO-OH cycle, which primarily determines the global tropospheric oxidizing capacity. This capability is important for capturing the nonlinear feedbacks of the CH_4-CO-OH system and understanding the perturbations to relatively long-lived methane and the concomitant impacts on climate. We implemented the ECCOH module into the NASA GEOS-5 Atmospheric Global Circulation Model (AGCM), performed multiple sensitivity simulations of the CH_4-CO-OH system over two decades, and evaluated the model output with surface and satellite datasets of methane and CO. The favorable comparison of output from the ECCOH module (as configured in the GEOS-5 AGCM) with observations demonstrates the fidelity of the module for use in scientific research.

1. Introduction

The coupled methane - carbon monoxide - hydroxyl radical (CH_4-CO-OH) system is nonlinear (e.g., Prather, 1994) and important in determining the troposphere's oxidizing capacity (e.g., Chameides et al., 1976). Methane is the second most important anthropogenic greenhouse gas (GHG), though its 100-year global warming potential (GWP) is 34 times larger than that for carbon dioxide (CO_2; Myhre et al., 2013). Methane is responsible for about 20% of the warming induced by long-lived GHG since pre-industrial times (Kirschke et al., 2013). The CH_4-CO-OH system has implications for tropospheric ozone and, subsequently, air quality (e.g., Fiore et al., 2002). A thorough understanding of historical methane, CO and OH trends and variations is necessary to credibly predict future changes and their climate feedback, as well as, to develop strategic national and international emission reduction policies.

The major limitation of forward modeling studies of trends and variability in the CH_4-CO-OH system is the computational expense associated with simulating ozone-nitrogen oxides-volatile organic compounds (O_3-NO_x-VOC) photochemistry for the determination of OH, particularly since perturbations to relatively long-lived methane (~8-10 y) can take several

decades to fully evolve (e.g., Prather, 1996). There are few forward modeling studies in the literature that carry a full representation of O_3-NO_x-VOC chemistry, though they necessarily present a limited number of sensitivity simulations (e.g., Fiore et al., 2006; Voulgarakis et al., 2015).

To overcome this computational expense, global modeling communities use archived, monthly OH fields to simulate the oxidation of methane and CO. Typically, the archived distributions are for one year and used for each year of the simulation. These distributions are taken from a global model simulation that carries a full representation of O_3-NO_x-VOC chemistry or climatology, such as was done by Wang et al. (2004) and in the TransCom methane model intercomparison project (Patra et al., 2011). In most cases, this implementation requires the adjustment of the OH levels, so that methane growth rates match those observed (e.g., Patra et al, 2011). Furthermore, simulated OH levels using full chemistry mechanisms in global models are still highly uncertain because of incomplete knowledge and representation of OH sources, sinks and recycling (e.g., Elshorbany et al., 2010b, 2012a, 2012b, 2014; Stone et al., 2012).

Limitations of using archived, monthly OH fields for studies of methane and CO's evolution are that feedbacks of the CH_4-CO-OH cycle on methane, CO and OH are not captured as the losses of methane and CO by reaction with OH are assumed to be linearly proportional to the OH fields. For methane, this assumption is acceptable on time scales shorter than its lifetime, but becomes less valid on multi-decadal time-scales (e.g., Prather, 1996). Chen and Prinn (2006) found that using an archived, annual cycle of OH may mask or bias the interannual changes of methane. For relatively short-lived CO (~1-2 months), this assumption is not valid given the strong feedback between CO and OH (e.g., Duncan and Logan, 2008; Voulgarakis et al., 2015). Therefore, there is a need for a computationally-efficient solution to simulate credible temporal and spatial distributions of OH over several decades, while capturing the nonlinear feedbacks of the CH_4-CO-OH system.

We have two primary objectives in this study. First, we present and validate the computationally-Efficient CH_4-CO-OH (ECCOH; pronounced like "echo") module to interactively simulate the chemistry of the CH_4-CO-OH system within a chemistry-climate model, carbon cycle model, or Earth System Model. The computational efficiency of the ECCOH module allows many sensitivity simulations of multiple decades to be performed, which is important for capturing the nonlinear feedbacks of the CH_4-CO-OH system and understanding the perturbations to methane and the concomitant impacts on climate. Second, we conduct a series of simulations, which we refer to as "scenarios" hereafter, using the ECCOH module as implemented in the NASA Goddard Earth Observing System, Version 5 Atmospheric General Circulation Model (GEOS-5 AGCM). The purpose of these scenarios is to attribute the influence of various factors on the observed spatial distributions and temporal evolutions of methane, CO, and OH. In Sect. 2, we describe the ECCOH module, model setup and sensitivity scenarios. In Sect. 3, we compare the simulated trends and variations of methane and CO in our reference scenario with in situ and satellite measurements. In our sensitivity scenarios, we explore the influences of several causal factors on the observed spatial distributions and temporal evolution of methane, CO, and OH (Sect. 4).

2 Technical Approach and Methodology

2.1 Description of the ECCOH Module and Its Implementation

The ECCOH module is composed of a parameterization of tropospheric OH and tracers of methane and CO. The advantage of the ECCOH module over a full representation of O_3-NO_x-VOC chemistry is computational efficiency. The computational cost of simulating tropospheric OH is reduced by about a factor of 500 when the full O_3-NO_x-VOC chemistry is replaced by a parameterization of OH (Duncan et al., 2000; Duncan et al., 2007a and references therein). This computationally-efficient parameterization of OH allows 1) for many multi-decadal model sensitivity simulations to be performed and 2) one to deconvolve the impact of various factors on the observed trends and variability in methane and CO. It was designed to be applicable to preindustrial, present day and possible future conditions (Duncan et al., 2000).

The parameterization of OH accurately represents OH predicted by a full chemical mechanism as a set of high-order polynomials in meteorological variables (i.e., pressure, temperature, cloud albedo), solar irradiance variables (i.e., ozone column, surface albedo, declination angle, latitude) and chemical variables (i.e., nitrogen oxides (as a family), ozone, water vapor, and various VOCs), including CO and methane. That is, the 24-hour average OH is calculated interactively in the model and responds to changes in the concentrations of trace gases and meteorology. We adjust the OH from the parameterization to account for important updates in kinetic and photolytic information of O^1D quenching reactions by water vapor, molecular nitrogen, and molecular oxygen (Sander et al., 2011). These reactions are key as the primary production pathway (P) for OH involves the formation of excited O^1D atoms by photolysis of ozone (O_3), followed by their reaction with water vapor in competition with their collisional quenching by reaction with molecular nitrogen and oxygen: $P = j[O_3] * 2k_1[H_2O] / (k_1[H_2O] + k_2[N_2] + k_3[O_2])$, where j is the ozone photolysis rate and k_1, k_2 and k_3 are the rate constants of O^1D reactions with water vapor, nitrogen and oxygen, respectively. Typically, this adjustment decreases OH by 10-30%, depending on altitude and season. The losses of methane and CO in the ECCOH module are determined by their reaction with tropospheric OH. Additional losses of methane in the stratosphere occur by reactions with OH, Cl and O^1D, whose distributions are simulated using archived, monthly fields. Stratospheric CO chemistry is simulated with archived loss and production rates (Duncan et al., 2007).

We implemented the ECCOH module into the Goddard Earth Observing System, Version 5 Atmospheric General Circulation Model (GEOS-5 AGCM, Fortuna version, Rienecker et al., 2008; Pawson et al., 2008; Ott et al., 2010; Molod et al., 2012). The AGCM combines the finite volume dynamical core described by Lin (2004) with the GEOS-5 column physics package, as summarized by Rienecker et al. (2008). The AGCM domain extends from the surface to 0.01 hPa and uses 72 hybrid layers that transition from terrain following near the surface to pure pressure levels above 180 hPa. We use a horizontal resolution of 2° latitude × 2.5° longitude and the time step is 30 minutes for physical computations.

2.2 Description of the Reference and Sensitivity Scenarios

For our study, we performed several model simulations using the ECCOH module in the GEOS-5 AGCM (see Table 1 and Table 2). The model setup (i.e., emissions, inputs to the parameterization of OH, and dynamics) of the reference scenario, which we refer to as the *Base* scenario, is detailed in Table 1. Compared to the sensitivity scenarios described in Table 2, the *Base* scenario is the least complex. For example, all CO emissions and natural methane emissions are for one year that are repeated for each year of the simulation (1988-2007); therefore, interannual variations in methane and CO levels caused by variations in these emissions will not be captured in the *Base* scenario. However, there are two important sources of variability that are included in the *Base* scenario. First, the dynamics are constrained by varying historical seas surface temperatures and sea ice concentrations. Therefore, the *Base* scenario will capture variations in methane, CO, and OH resulting from meteorological variations, such as those associated with the El Niño Southern Oscillation (ENSO). In addition, the atmospheric temperature, pressure and specific humidity are calculated online by the GEOS-5 AGCM and are fed into the parameterization of OH as the runs progress, so interannual variations in water vapor, temperature, and cloud cover are also included in the *Base* scenario. These factors are known to influence variations in OH and thus CO and methane (e.g., Duncan and Logan, 2008; Holmes et al., 2013). Second, interannual variations in anthropogenic methane sources are included in the *Base* scenario. In Sect. 3, we evaluate model output from the *Base* scenario with the observational datasets described in Table 3.

We present the results of our sensitivity scenarios in Sect. 4. We explore the influences of several causal factors on the observed spatial distributions and temporal evolutions of methane, CO, and OH. These causal factors include annually-varying emissions (i.e., natural methane emissions, anthropogenic and natural CO emissions, see Figure S 1 and Figure S 2) and input variables to the parameterization of OH (Table 2).

3 Evaluation of the Base Scenario

We evaluate the model output of methane and CO from the *Base* scenario (Table 1) with satellite and in situ observations (Table 3). We also compare simulated OH with that from a GESO-5 AGCM simulation (with a full representation of O_3-NO_x-VOC chemistry) that was included in the Atmospheric Chemistry and Climate Model Intercomparison Project (ACCMIP, Lamarque et al., 2013). In Sect. 4.2, we compare the simulated OH anomaly to that inferred from MCF data (Montzka et al., 2011). We highlight where this *Base* scenario's simplicity results in a poor or satisfactory comparison of the model output with the observed temporal and spatial distributions of methane, CO, and OH. We demonstrate that the ECCOH module for this scenario reasonably captures the distributions of methane and CO, within the limitations of this scenario, as compared to measurements and other model studies (e.g, Shindell et al. 2006; Patra et al., 2011; Naik et al., 2013).

3.1 Tropospheric OH

It is well established that simulated OH varies widely between models (Shindell et al.,

2006; Fiore et al., 2009; Voulgarakis et al., 2013). For instance, Voulgarakis et al. (2013) found that simulated tropospheric methane lifetimes of various models ranged from ~7 to ~14 years; this spread is similar to that calculated by Shindell et al. (2006) and Fiore et al. (2009), even when all participating models used identical methane abundances and CO emissions (Shindell et al., 2006). Shindell et al. (2006) related the wide spread of simulated CO between models to the large spread in simulated OH.

This wide spread in simulated OH between models is the result of several factors. First, there are very few direct observations of OH to constrain models (e.g., Stone et al., 2012) and none on regional or global scales. Therefore, the methylchloroform (MCF) lifetime serves as a widely used, indirect proxy for global OH abundance (e.g., Lawrence, 2001). Though useful, the MCF lifetime gives an incomplete description of the spatial and vertical distributions of OH (e.g., Lawrence, 2001) and there are uncertainties concerning MCF emissions and the subsequent lifetime (e.g., Wang et al., 2008). Second, there are large uncertainties in photochemical kinetic data important for the simulations of OH chemistry (e.g., Shindell et al., 2006; Elshorbany et al., 2012b). For instance, Elshorbany et al. (2012b) showed that simulated nitrous acid (HONO) concentrations are largely underestimated by up to an order of magnitude as compared to measurements, which can lead to a significant underestimation of OH, especially in urban regions with high NO_x levels. Also, in unpolluted, forested environments, significant discrepancies exist between models and measurements (Stone et al., 2012). Third, there are other factors that influence OH and significantly differ between models (e.g., water vapor, clouds, overhead ozone column, etc.; Shindell et al., 2006).

We present our simulated OH from the *Base* scenario and, despite the challenges concerning OH discussed above, we show here and in Sect. 4.2 that our simulated global mean OH and spatial/vertical distributions are reasonable relative to the MCF proxy for OH as well as simulated OH from other models. Seasonal, zonal mean OH vertical distributions for the *Base* scenario are shown in Figure 1. Related to the OH dependency on UV radiation (Rohrer and Berresheim, 2006), the maximum and minimum OH levels at any given location occur in local summer and winter, respectively (Figure 1). OH maximizes around 600 hPa because of vertical dependencies of the main sources and sinks of OH (Spivakovsky et al., 1990). The seasonal and spatial distributions of the zonal mean OH in the *Base* scenario are quite comparable to the OH climatology of Spivakovsky et al. (2000).

The seasonal, mean OH global distributions at 850 mbar for the entire simulation period (1988-2007), as well their standard deviations, for the *Base* scenario are shown in Figure 2. The overall interannual variations in OH (given by the annual mean standard deviation) are small (<5%) and mainly related to meteorological variations (e.g., water vapor, clouds, temperature, and transport) as annually-repeating emissions are used in the *Base* scenario, except for anthropogenic methane emissions (Table 1, Figure S 1, Figure S 2). This result is consistent with Voulgarakis et al. (2013) who show that OH has the strongest relationship with changes in temperature and humidity when emissions do not vary interannually. As discussed in Sect. 4 we see considerably larger variations in OH in several of our sensitivity simulations, which have interannual variations in methane and CO emissions as well as in OH constraints.

The *Base* scenario's global, mean MCF lifetime with respect to tropospheric OH ranges

from 5.03 (±0.49) to 5.39 (±0.52) years over the simulation period. The lifetime in the southern hemisphere ranges from 5.85 (±1.51) to 6.33 (±1.65)) and in the northern hemisphere from 5.20 (±1.90) to 5.52 (±2.0)). The global mean lifetime with respect to OH is within values reported in the literature (e.g., 5.7(±0.9) in Naik et al. (2013)). The annual mean tropospheric global mean lifetime of methane ranges from 8.52(±0.84) to 9.15 (±0.91) years over the simulation period. These values are also well within those reported in previous multimodel comparison studies (e.g., 9.7±1.7 yr (Shindell et al., 2006); 9.7±1.5 yr (Naik et al., 2013)).

We also compare our simulated OH with that from a GEOS-5 AGCM simulation that carries a full representation of O_3-NO_x-VOC chemistry. This simulation was included in the Atmospheric Chemistry and Climate Model Intercomparison Project (ACCMIP, Lamarque et al., 2013; the model was designated as "GEOSCCM"). Henceforth we refer to this simulation as the "ACCMIP simulation". The same CO emissions (annually-repeating emissions for year 2000; Table 1) are used in both the *Base* and ACCMIP simulations, but there are differences between the simulations (e.g., model dynamics, prescribed methane, etc.). Despite these differences, we find that the spatial and vertical distributions of OH are quite similar between the simulations with differences generally less than 10% (Figure S 23). The global mean tropospheric OH in the *Base* scenario of 10.9×10^5 molecules cm^{-3}, compares also well with that of 11.4×10^5 molecules cm^{-3}, from the ACCMIP simulation as well as within the range of means from other models (e.g., 6.5 – 13.4 $\times 10^5$ molecules cm^{-3} (Voulgarakis et al., 2013)). We further provide a comparison of our simulated OH anomaly to that inferred from MCF measurements (Montzka et al., 2011) in Sect. 4.2.

3.2 Methane

GMD surface data: We evaluate our simulated surface distributions of methane from the *Base* scenario with data from the NOAA Global Monitoring Division (GMD) network (Table 3). The simulated interannual variation of methane's global growth rate agrees reasonably well with that estimated from GMD data, using all available data from 92 stations over the simulation period 1988-2007 (Figure 3), except for the 1997/1998 event. This result implies that interannual variations in anthropogenic emissions explain much of methane's growth rate over the study period, the findings of the TransCom model intercomparison project (Patra et al., 2011).

Overall, the comparison of model output and data at individual GMD stations is favorable. Figure 4 to Figure 7 show comparisons for monthly averages, seasonal averages, and annual differences, respectively, at six GMD stations, which were chosen as they have long time records. The correlation slope (S) and coefficient (R^2) for these six stations (Table 4) range from 0.56 to 0.79 and from 0.58 to 0.91, respectively, with the agreement generally improving from the northern to southern hemispheres.

There are two important features of the observations that are not simulated in the Base scenario. First, the *Base* scenario overestimates methane concentrations by 20-30 ppbv at the northern high latitude stations of Alert and Barrow during the 1980s and 1990s (Figure 4-Figure 6 and Figure S 7). The overestimation of methane in the northern hemisphere during the 1990s occurs because of regional high biases in the natural methane emissions (see Patra

et al., 2011). As shown in Sec. 4, simulated methane improves significantly in the northern hemisphere in the $E_{CH4}Vary$ scenario, which includes annually-varying natural methane emissions. Second, the *Base* scenario captures the increasing observed methane trend in the 1990s, but underpredicts methane levels in the 2000's. Both of these features (i.e., high bias at high northern latitudes in the 1990's and low bias in the 2000's) are consistent with the findings of the TransCom model intercomparison project that used the same methane emissions (Table 1 and Patra et al., 2011). One additional feature, is that the simulated methane growth rate does not capture the 1997/1998 El Nino anomaly (Figure 7).

SCIAMACHY methane: We compare the simulated methane dry columns to those from SCIAMACHY (**Table 3**, Figure 8). The data have the best spatial coverage during boreal summer because of lower cloud cover during this season (Schneising et al., 2011). The observed methane dry column levels (Figure S 8) reach their highest levels during boreal summer and fall, maximizing over Asia (eastern China and northern India) because of high emissions from wetlands and rice paddies in those seasons. The *Base* scenario reproduces the spatial distribution of the data well with a bias of < 2% over most of the globe, except during boreal summer where it is biased low, but still within the measurement uncertainties (~7-10%; Gloudemans et al., 2008; Houweling et al., 2014). Houweling et al. (2014) demonstrates that SCIAMACHY data have a seasonal bias that ranges from about -50 ppb during boreal winter to about +50 ppb during boreal summer as compared to the Total Carbon Column Observing Network (TCCON) measurements, which may also explain the simulated seasonal biases mentioned above (Figure 8).

3.3 CO

GMD surface data: The *Base* scenario captures the monthly variability of GMD CO data well with a mean correlations slope (S) and coefficient (R^2) of 0.83 and 0.77, respectively, with the agreement improving generally from north to south (Figure 9 to Figure 11, Table 4). This result indicates that seasonal CO cycle is well captured in the *Base* scenario (Figure 11), which includes annually-repeating, but seasonally-varying biomass burning emissions (Figure S 2). As expected, the simulation does not capture the significant interannual variations (Figure 9, Figure 10). The low biases reach ~40 ppb in boreal winter and spring at high northern latitudes (**Error! Reference source not found.**). During the 1980's and 1990's, CO levels in the northern hemisphere declined substantially because of changing patterns of emissions (Duncan et al., 2007a), which is not simulated with the annually-repeating CO emissions used in the scenario (Figure S 2). These results are in agreement with the findings of the multi-model ACCENT study (using annually-repeating CO emission), in which there was a low bias of ~50 ppbv at northern hemisphere high latitude stations (Shindell et al., 2006).

MOPITT and TES/MLS CO: The primary advantage of satellite data, above ground-based networks, is spatial coverage, so we compare the spatial and seasonal distributions of simulated CO with those from the MOPITT and TES/MLS instruments (Figure 12-Figure

13 and Figure S 14 to **Error! Reference source not found.**). The distributions of CO from the *Base* scenario compare well overall with data. The mean biases relative to both datasets are within ±10% over most of the globe and in all seasons. For example, the seasonal correlation slopes (S) range from 0.75 to 0.98 and coefficients (R^2) range from 0.80 to 0.98, respectively, between MOPITT, TES/MLS data and the *Base* scenario output (Figure S 16 and Figure S 18) with the agreement generally best during boreal winter and lowest during the boreal summer. However, the largest biases (see Figure 12 and Figure S 15) occure over 1) biomass burning regions (>20%) during boreal winter, indicating that either the CO emissions used in the *Base* scenario are too high or that simulated OH is too low, and 2) most of the northern hemisphere (< -20%) during the summer season, indicating that either CO emissions are too low or that OH levels are too high, which is consistent with previous studies using similar emissions (e.g., Shindell et al., 2006; Strode et al., 2015). In addition to possible biases associated with emissions, some of the model-observation discrepancies may be associated with uncertainties in the satellite datasets (Ho et al., 2009; Deeter et al., 2012; Amnualojaroen et al., 2014). Deeter et al. (2012) found that the bias in the MOPITT a priori in some stations over the US exhibits a clear seasonal cycle, highest in winter and lowest in summer (Deeter et al., 2012), in agreement with our results. Amnualojaroen et al. (2014) found that simulated CO concentrations are significantly and consistently higher than that of MOPITT V6 data over areas of biomass burning in Southeast Asia, similar to our results.

The primary advantage of the TES/MLS joint CO product is that it gives information on vertical distributions (Figure 13). The simulation captures the tropospheric vertical profiles reasonably well (within ±1σ of TES/MLS mean) at the selected locations in the northern and southern hemispheres and in all seasons, except over West Africa in boreal winter during the peak of biomass burning. The adjustment of the simulated CO with the TES/MLS averaging kernel (AK) significantly improves the agreement over all locations and in all seasons though simulated CO is still biased high over West Africa by ~50% during the peak of biomass burning. However, as mentioned earlier, known uncertainties in the TES/MLS retrieval metrics, emissions and OH chemistry may contribute to the scenario's bias.

4 Evaluation of the Sensitivity Scenarios

In Sect. 4.1, we present the results of our sensitivity scenarios (Table 2). We discuss the contribution of the various factors to the simulated spatial distributions and temporal evolution of methane, CO, and OH. In Sect. 4.2, we discuss the interannual variations of OH. In Sect. 4.3, we investigate the spatial and temporal distribution of methane and CO loss rates with respect to OH. In Sect. 4.4, we discuss the global variations of methane, CO and OH for the *Base* and *AllVary* scenarios.

4.1 Factors that Influence Methane, CO, and OH

The differences in global abundances of CO and OH between our least complex (*Base*) and most complex (*AllVary*) scenarios are substantial and their impact on methane's evolution is nontrivial. Figure 22 shows the mass-weighted anomalies of OH, CO and methane (relative to their mean concentrations during the simulation period, 1988-2007) for the *Base* and *AllVary* scenarios. The magnitudes of the anomalies are substantially larger for

CO and OH and modestly so for methane in the *AllVary* scenario for all regions of the globe. In the following paragraphs, we discuss the contribution of the various factors to the observed spatial distributions and temporal evolution of observed methane, CO, and OH at the GMD stations. We highlight the improvement (or worsening) of each scenario's output with the observed temporal and spatial distributions of methane and CO (Table 3) as compared to the *Base* scenario.

E_{CH4}Vary Scenario: In the *Base* scenario, annually-repeating natural sources (i.e., wetlands and biomass burning) of methane and annually-varying anthropogenic sources are used (Table1). In the *E_{CH4}Vary* scenario, all methane emissions are annually-varying (Figure S 1). Variations in emissions from wetlands, particularly tropical ones, are the largest single contributor to global interannual variations, with biomass burning being a lesser contributor (e.g., Bousquet et al., 2006). Patra et al. (2011) reported that up to 60% of methane's observed interannual variation can be explained by variations in meteorology as well as interannual variations in wetland and biomass burning emissions. Given the high methane background concentration, the spatial differences of methane tropospheric columns between the *E_{CH4}Vary* and *Base* scenarios are rather small (about ±5 ppb (-1 to 1%)) over most of the globe when taken as seasonal averages of 1988-2007 (Figure S 26 to Figure S 29). Consistent with the annually-varying natural emissions of methane, the largest differences occurred over the rice-producing regions of India and Bangladesh (up to ~5%)) and the wetlands of South America (down to -5%), including the Pantanal. The impact of annually-varying natural methane emissions has a small effect (-1% to 1%), as expected, on the spatial distributions of the tropospheric columns of CO and OH because of the slow reaction rate of methane with OH (Figure S 26). The simulated interannual variability of methane's global growth rate agrees better than the rate from the *Base* scenario with the observed rate, especially during the 1997/1998 large biomass burning events (Figure 3). The simulated methane monthly variations from the *E_{CH4}Vary* scenario are in much better agreement with the northern hemisphere high latitude GMD station observations as compared to the *Base* scenario (Figure 5 to Figure 7 and Figure S 3), which is also consistent with the findings of the TransCom exercises (Patra et al., 2011). The correlation slope, averaged over northern hemisphere stations, improves from 0.54 in the *Base* scenario to 0.71 for the *E_{CH4}Vary* scenario, with a slight improvement in the correlation coefficient (Table 4). The simulated growth rate improves significantly (e.g., during 1997 and 1998 (Figure 7). Including variable methane emissions (E_{CH4}Vary) has on only minor impacts on simulated CO surface concentrations (Table 4; Figure 9).

BBE_{CO}Vary, FFE_{CO}Vary, $FFBBE_{CO}$Vary Scenarios: We developed three scenarios to understand the influence of annually-varying CO emissions from biomass burning and fossil fuels combustion (Figure S 2) on the observed interannual variation of methane, CO and OH. As discussed in Sect. 3.3, simulated CO levels in the *Base* scenario are generally underestimated, especially at northern hemisphere stations, which is related to the annually-repeating emissions not reflecting important changes in anthropogenic emissions over the study period. In addition, the interannual variability of CO, such as associated with variations in biomass burning, is not captured in the *Base* scenario. Including annually-varying biomass burning emissions (*BBE_{CO}Vary*) significantly improves the agreement of

the simulated CO with GMD observations (mean S=0.85, R^2 = 0.74, Table 4), such as during years with large fires (e.g., 1997, 1998, 2003, 2004; Figure 9 to Figure 11). Adding annually-varying anthropogenic CO emissions in addition to annually-varying biomass burning emissions (*FFBBE$_{CO}$Vary*) further improves the comparison (mean S=0.91, Table 4), particularly in the northern hemisphere during the 1990s (Figure 10).

Simulating annually-varying CO biomass burning emissions (i.e., *BBE$_{CO}$Vary* scenario) improves simulated methane relative to the *Base* scenario as compared to observations (mean S=0.93, R^2= 0.76, Table 4). This high correlation slope in the *BBE$_{CO}$Vary* scenario reflects the model skill in capturing the month-to-month variations as can also be inferred from the well-simulated growth rate in Figure 7, especially during the 2000s, but not the absolute simulated concentrations. Simulated methane levels by the *BBE$_{CO}$Vary* scenario (see Figure S 4) are overestimated. This is due, in part, to using annually-varying CO biomass burning emission but annually-repeating anthropogenic emissions (Table 1, Figure S 2). Including both annually-varying fossil fuel and biomass burning emissions significantly improves the comparison of the *FFBBE$_{CO}$Vary* scenario (Figure S 5) compared to the *BBE$_{CO}$Vary* scenario, though still overestimating methane during the 1990s, especially in the northern hemisphere. However, including anthropogenic emission reduces the agreement (*FFBBE$_{CO}$Vary* scenario, S=0.64, R^2=0.54), which is due to the overestimated methane levels during the 1990s. Overestimated methane levels compared to the *Base* scenario may due to regionally biased CO emissions.

It is important here to mention also the limitation of the GMD stations, which are located in remote area and their monthly mean data exclude the non-background methane and CO levels. Increased CO emissions in polluted air deplete OH and thus lead to increased methane levels that have much higher lifetime and thus affect the methane levels at these remote sites but not essentially CO, which have much shorter lifetime. Thus, it appears that methane measured at the remote sites is more sensitive to changes or biases in CO emission that originate from polluted regions than measured CO at these remote sites. Bian et al. (2008) report the relative insensitivity of CO at GMD stations to rather large changes in biomass burning emissions. They attribute this to the remote locations of the stations and the relatively short lifetime of CO. However, methane's lifetime is sufficiently long so methane levels at the GMD stations would be more sensitive to distant perturbations. This may explains the simulated higher methane levels in the *FFBBE$_{CO}$Vary* scenario compared to the Base scenario.

Overall, annually-varying CO emissions (*FFBBE$_{CO}$Vary*) have a significant impact on the spatial distributions of tropospheric CO (±20%) and OH (±10%) relative to the *Base* scenario, but a relatively small influence (±1%) on methane (Figure S 27, Table 4).

OH$_{input}$Vary Scenario: In this scenario, we look at the impact of other causal factors that influence OH, including trends in NO_x and VOC emissions and the overhead ozone column. Both variations in the overhead ozone column and NO emissions from lightning are known to cause variations in global OH (e.g., Duncan and Logan, 2008; Murray et al., 2013). Together, these causal factors have a significant influence on the spatial distributions of tropospheric OH (±20%) and CO (±5%) relative to the *Base* scenario, but a relatively small influence (±1%) on methane (Figure S 27; Table 4).

Variable casual factors in this scenario lead to overestimated methane levels during the 1990s, compared to the *Base* scenario (Figure S 6, Figure 6). This is likely due to overestimated NO_x levels (i.e., in polluted regions), which deplete OH (i.e., NO_2+OH=HNO_3) and thus higher methane levels. As aforementioned, owing to the high methane lifetime, it reaches and affects methane levels at these GMD remote stations. However, there is little impact on the comparison of simulated CO with observations at the selected six GMD stations (Figure 10), which have been shown to be insensitive to large changes in biomass burning emissions because of their remote locations from source regions (Bian et al., 2008). Thus, it is clear that the interannual variations of these causal factors convolved in the $OH_{input}Vary$ scenario, strongly contribute to the overall variations in OH, CO and methane, such as also shown in Duncan and Logan (2008) for CO and OH, and should be simulated when studying the evolution of the CH_4-CO-OH cycle over time.

AllVary Scenario: In this scenario, we investigate the combined effect of all variables (Table 2) on the simulated distributions of methane, CO, and OH. Given the large differences in the spatial distributions of methane (±5%), CO (±20%), and OH (±20%) between the *Base* and *AllVary* scenarios (Figure S 28, Table 4), this scenario illustrates the limitation of using a static distribution of annually-repeating OH and emissions for studying the complex and non-linear CH_4-CO-OH cycle..

The global mean tropospheric MCF lifetime for the *AllVary* scenario does not change significantly from that of the *Base* scenario, ranging from 4.96 (±0.41) to 5.50 (±0.49) years for the entire simulation period, despite the large spatial changes in OH (see below). However, the MCF lifetime in the southern hemisphere reaches a maximum of 6.62 (±1.69) years in 1992 which is about 8% higher than the corresponding value (6.13±1.61) years in the *Base* scenario, which can be explained by the increase of biomass burning emissions in the *AllVary* scenario. In the northern hemisphere, the MCF lifetime is slightly lower reaching its minimum of 4.92 (±1.65) years in 2001 (about 6.5% lower than that in the base scenario of 5.24 (±1.88)) due to the decreased anthropogenic emissions including CO (see Figure S 2). Also, the mean tropospheric global methane lifetime ranges from 8.42 (±0.72) to 9.33 (±0.85) years for the *AllVary* scenario, which is similar to the value obtained using the *Base* scenario and consistent with previous literatures (Sect. 3.1).

4.2 OH Interannual Variability

We compare simulated, mass-weighted pseudo first order rate constants (k'), a proxy for OH interannual variations, from each of our scenarios (Table 1-Table 2) to that inferred from MCF measurements (1998-2007; Montzka et al., 2011). We find that none of our model scenarios are able to reproduce the inferred interannual OH variability of Montzka et al. (2011), though the simulated variability is of similar magnitude and within observational uncertainty (Figure 15). Our findings are consistent with other modeling studies (Montzka et al., 2011; Holmes et al., 2013; Murray et al., 2013 and references therein). While global interannual variations are informative, there can be considerable OH interannual variations regionally (Section 4.1) that may not be reflected in the global average (Lelieveld et al., 2002; Wild and Palmer, 2008).

Despite the lack of agreement between the inferred and simulated OH variations, this

464 comparison exercise allows us to understand the contribution of various factors to the
465 simulated interannual variations of tropospheric OH and, subsequently, the lifetimes of
466 methane and CO. Figure 15 shows that the *Base* scenario has ±3% interannual variability.
467 This scenario includes interannual variations in meteorology, such as in clouds, water vapor,
468 temperature and solar radiation, which are known to be important drivers of OH (e.g., Rohrer
469 et al., 2006; 2014). The only large deviation in OH from the *Base* scenario occurs in 1997
470 and 1998 in the $BBE_{CO}Vary$ scenario that reflects the impact of interannual variations of
471 biomass burning CO emissions. There were several major wildfire events that account for
472 this deviation, including fires in Indonesia, Mexico, and the boreal forests of Asia and North
473 America (e.g., Duncan et al., 2003a). For instance, Duncan et al. (2003b) used a model to
474 show that the Indonesian wildfires in 1997 depressed OH levels by more than 20% over the
475 Indian Ocean and 5-10% over much of the tropics for several months.
476

477 ## 4.3 Spatial and Temporal Distributions of the Production/Loss Rates of
478 Methane and CO

479 Even though methane is relatively well mixed in the troposphere due to its long lifetime,
480 there is important spatial and vertical heterogeneity in methane's loss rate (Figure 16 to
481 Figure 21), which is associated with the distribution of methane's sources, methane's
482 reaction with OH, and changes in the density of air with altitude. The global methane loss
483 rate maximizes during boreal summer and reach minimum during the boreal winter (Figure
484 16). Most methane loss occurs between 30°S and 30°N (Figure 16) as most methane sources
485 are found in this latitude band and because of the methane's reaction with OH being
486 temperature dependent (Sander et al., 2011). In addition, most loss occurs near the surface
487 despite higher OH concentrations in the mid-troposphere (Figure 1) because of the altitude
488 dependence of air density and also the temperature dependence of the loss rate (Figure 17).
489 Simulated methane loss rates in the *AllVary* scenario have much higher spatial variability
490 than in the *Base* scenario (Figure 18). In contrast to methane, a higher proportion of CO is
491 lost at northern hemisphere mid-latitudes as the CO loss rate is less temperature dependent
492 than methane's, the lifetime is shorter and a greater proportion of CO sources are found there
493 (Figure 19). Given the shorter lifetime of CO (~1-2 months), there is considerably more
494 spatial structure in the distribution of the CO loss rates than for methane. CO loss rate show
495 also a strong vertical gradient that relates mainly to variability in CO vertical distribution
496 (Figure 20). The simulated seasonal mean loss rates of CO by *AllVary* scenario has much
497 higher variability that reaches up to ~20% compared to about 5% in the *Base* scenario
498 (Figure 21). These results show also that CO is less sensitive to small natural variability in
499 OH compared to methane, consistent with previous studies (e.g., Naik et al., 2013 and
500 references therein).

501 ## 4.4 Global Variations of Methane, CO and OH

502 In this section, we compare the large-scale variations of methane, CO, and OH between our
503 least (*Base*) and most (*AllVary*) complex scenarios. **Figure 22** shows the anomalies of mass
504 weighted concentrations of OH, CO and methane for both the *Base* and the *AllVary*

505 scenarios. The magnitudes of the year-to-year anomalies in methane are not substantially
506 different between the two scenarios, though the *Base* scenario includes the important source
507 of variation associated with anthropogenic methane emissions. On the other hand, the
508 anomalies for CO and OH are far greater in the *AllVary* scenario. The magnitude of the CO
509 anomalies is a factor of ten greater in the *AllVary* scenario than the *Base* scenario, which has
510 constant CO emissions. The magnitude of the OH anomalies increase from about ±2% to
511 ±5%, though as we discussed earlier, there are much larger variations on regional scales that
512 are masked in the global average. In general, CO and OH anomalies are coincident, but of
513 opposite sign as reaction of CO with OH is the primary sink for both gases on a global scale.
514 Similar anomalies are seen in the mid-latitudes of both hemispheres, indicating the global
515 extent of some specific events, such as large biomass burning events. These results are also
516 consistent with Voulgarakis et al. (2015) who, using full chemistry simulations, found large
517 anomalies (> 15%) in CO using variable CO biomass burning emissions compared to
518 constant emissions.
519 The El-Niño Southern Oscillation (ENSO) is an important phenomenon that affects,
520 among others, the variability of sea surface temperatures and water vapor, which may thus
521 affect the OH production and variability via O_3 photolysis and the subsequent reaction of
522 excited oxygen molecules (O^1D) with water vapor. We investigate this process via the
523 relation between the anomaly of the mass weighted OH and the Multivarient Enso Index
524 (MEI, Wolter et al., 2011) as a proxy of the ENSO. As mentioned earlier, variations in the
525 OH due to large El-Ñino/La-Ñina events may not be apparent or may even change sign if
526 coincident with other important factors, e.g, anthropogenic or biogenic emissions (see also
527 Murray et al., 2013 and above). Therefore, for this correlation, we use the reference scenario
528 (*Base*) with fixed emissions to avoid masking the natural IAV related to the meteorological
529 variations with strong emission IAVs. Figure 23 show the mass weighted OH anomalies
530 compared to the MEI index, integrated both globally and over the El-Nino 3.4 region
531 (zoomed over the period 1998-2007 for clarity). As shown in Figure 23, the anomalies of the
532 mass weighted OH compared generally well to the MEI index and also capturing most of the
533 IAV details. Most apparently, is the correlation in 1997-1998 during the major El-Ñino
534 episodes as well as the weaker 2003-2004 events. La Ñina events in 1988-1989, 1995, 1998-
535 1999 are also well captured. The decrease in OH anomalies during 2007-2008 is also well
536 captured albeit overestimated. Including the variable emissions of CO and OH constraints
537 worsen the correlations and mask several important features, in agreement with previous
538 reports (e.g., Murray et al., 2011) and as mention earlier. However, including IAV in
539 methane (given by the $E_{CH4}Vary$ scenario) was found not to affect the OH interannual
540 variability, which is expected given the very long lifetime of methane relative to OH, but in
541 contrast to Montzka et al. (2011), who reported that the inter-annual variability of methane
542 may affect and reduce the OH inter annual variability.

543 5 Summary

544 We present the fully interactive, computationally Efficient CH_4-CO-OH module
545 (ECCOH), which we implemented into the NASA GESO-5 AGCM. We exercised the
546 module with a set of scenarios to simulate the influence of various causal factors on OH and

547 the observed variations in methane and CO over 1988-2007. The results of our exercises are
548 consistent with the findings of model intercomparisons and other studies in the literature.
549 The output from our various scenarios from 1988-2007 compares well with in situ and
550 satellite observations within their uncertainties. The spatial distributions and temporal
551 variations of 1) methane and CO are consistent with observations from the SCIAMACHY,
552 MOPITT, and TES-MLS satellite instruments and the GMD surface network, and 2) OH as
553 inferred from MCF data, which gives confidence in the fidelity of the ECCOH module for
554 use in scientific research. Discrepancies between the output from ECCOH and observations
555 are largely explained by known deficiencies (as reported in the literature) in the methane and
556 CO emissions used as input to the ECCOH module.
557
558 *Acknowledgements*: This work was supported by the NASA Modeling, Analysis and
559 Prediction and Interdisciplinary Science programs. We would like to thank the
560 SCIAMACHY WFM-DOAS team at the University of Bremen IUP/IFE for using their
561 methane L3 product as well as the TES/MLS Aura team for using their L2 CO product and
562 Stephen Montzka (NOAA) for providing MCF-inferred OH anomalies for comparison.
563 MOPITT CO column data were obtained from the NASA Langley Research Center
564 Atmospheric Science Data Center. Earlier model development of the ECCOH module by
565 Elena Yegorova is appreciated. Useful discussions with Huisheng Bian (NASA), Parbir
566 Patra (RIGC/JAMSTEC), Junhua Liu (NASA) and Jerald Ziemke, as well as, technical
567 support from Michael Manyin (NASA), Yasuko Yoshida (NASA) and Eric Nielsen (NASA)
568 are gratefully acknowledged.
569
570 **References**
571 Amnuaylojaroen, T., Barth, M. C., Emmons, L. K., Carmichael, G. R., Kreasuwun, J.,
572 Prasitwattanaseree, S., and Chantara, S.: Effect of different emission inventories on
573 modeled ozone and carbon monoxide in Southeast Asia, Atmos. Chem. Phys., 14, 12983-
574 13012, doi:10.5194/acp-14-12983-2014, 2014.
575 Bey, I., D. J. Jacob, R. M. Yantosca, J. A. Logan, B. D. Field, A. M. Fiore, Q. Li, H. Y. Liu,
576 L. J. Mickley, and M. G. Schultz (2001), Global modeling of tropospheric chemistry with
577 assimilated meteorology: Model description and evaluation, J. Geophys. Res., 106(D19),
578 23073–23095, doi:10.1029/2001JD000807.
579 Bousquet, P., Hauglustaine, D. A., Peylin, P., Carouge, C., and Ciais, P.: Two decades of OH
580 variability as inferred by an inversion of atmospheric transport and chemistry of methyl
581 chloroform, Atmos. Chem. Phys., 5, 2635-2656, doi:10.5194/acp-5-2635-2005, 2005.
582 Bousquet, P., Ciais, P., Miller, J. B., Dlugokencky, E. J., Hauglus- taine, D. A., Prigent, C.,
583 Van der Werf, G. R., Peylin, P., Brunke, E. G., Carouge, C., Langenfelds, R. L., Lathiere,
584 J., Papa, F., Ra- monet, M., Schmidt, M., Steele, L. P., Tyler, S. C., and White, J.:
585 Contribution of anthropogenic and natural sources to atmospheric methane variability,
586 Nature, 443, 439–443, 2006.
587 Bousquet, P., Ringeval, B., Pison, I., Dlugokencky, E. J., Brunke, E.-G., Carouge, C.,
588 Chevallier, F., Fortems-Cheiney, A., Frankenberg, C., Hauglustaine, D. A.,
589 Krummel, P. B., Langenfelds, R. L., Ramonet, M., Schmidt, M., Steele, L. P., Szopa, S.,
590 Yver, C., Viovy, N., and Ciais, P.: Source attribution of the changes in atmospheric

591 methane for 2006–2008, Atmos. Chem. Phys., 11, 3689-3700, doi:10.5194/acp-11-3689-
592 2011, 2011.
593 Buchwitz, M., de Beek, R., Burrows, J. P., Bovensmann, H., Warneke, T., Notholt, J.,
594 Meirink, J. F., Goede, A. P. H., Bergamaschi, P., Körner, S., Heimann, M., and Schulz, A.:
595 Atmospheric methane and carbon dioxide from SCIAMACHY satellite data: initial
596 comparison with chemistry and transport models, Atmos. Chem. Phys., 5, 941-962,
597 doi:10.5194/acp-5-941-2005, 2005.
598 Buchwitz, M., M. Reuter, O. Schneising, H. Boesch, S. Guerlet, B. Dils, I. Aben, R.
599 Armante, P. Bergamaschi, T. Blumenstock, H. Bovensmann, D. Brunner, B. Buchmann,
600 J.P. Burrows, A. Butz, A. Chédin, F. Chevallier, C.D. Crevoisier, N.M. Deutscher, C.
601 Frankenberg, F. Hase, O.P. Hasekamp, J. Heymann, T. Kaminski, A. Laeng, G.
602 Lichtenberg, M. De Mazière, S. Noël, J. Notholt, J. Orphal, C. Popp, R. Parker, M.
603 Scholze, R. Sussmann, G.P. Stiller, T. Warneke, C. Zehner, A. Bril, D. Crisp, D.W.T.
604 Griffith, A. Kuze, C. O'Dell, S. Oshchepkov, V. Sherlock, H. Suto, P. Wennberg, D.
605 Wunch, T. Yokota, Y. Yoshida, The Greenhouse Gas Climate Change Initiative (GHG-
606 CCI): Comparison and quality assessment of near-surface-sensitive satellite-derived CO2
607 and CH4 global data sets, Remote Sensing of Environment,.doi:10.1016/j.rse.2013.04.024,
608 2014.
609 Chameides, W., Liu, S. C. and Cicerone, R. J.: Possible variations in atmospheric methane, J.
610 Geophys. Res., 81, 4997-5001, 1976.
611 Chin, M., Ginoux, P., Kinne, S., Torres, O., Holben, B. N., Duncan, B. N., Martin, R.
612 V.,Logan, J. A., Higurashi, A., and Nakajima, T.: Tropospheric aerosol optical thickness
613 from the GOCART model and comparisons with satellite and sunphotometer
614 measurements, J. Atmos. Sci., 59, 461-483, 2002.
615 Dalsøren, S. and Isaksen, I. S. A.: CTM study of changes in tropospheric hydroxyl
616 distribution 1990- 2001 and its impact on methane, Geophys. Res. Lett., 33, L23811,
617 doi:10.1029/2006GL027295, 2006.
618 Deeter, M. N.: MOPITT (Measurement of Pollution in the Troposphere) Version6 Product
619 User'sGuide, available at: http://www2.acd.ucar.edu/sites/default/files/mopitt/v6_users_
620 guide_201309.pdf (last access: May 28th 2015), 2013.
621 Deeter, M. N., Worden, H. M., Edwards, D. P., Gille, J. C., and Andrews, A. E.: Evaluation
622 of MOPITT retrievals of lowertropospheric carbon monoxide over the United States, J.
623 Geophys. Res., 117, D13306, doi:10.1029/2012JD017553, 2012.
624 Dlugokencky, E. J., Bruhwiler, L., White, J. W. C., Emmons, L. K., Novelli, P. C., Montzka,
625 S. A., et al. (2009). Observational constraints on recent increases in the atmospheric CH4
626 burden. Geophysical Research Letters, 36, L18803, doi: 10.1029/2009GL039780, 2009.
627 Dlugokencky, E.J., P.M. Lang, and K.A. Masarie, Atmospheric Methane Dry Air Mole
628 Fractions from the NOAA ESRL Carbon Cycle Cooperative Global Air Sampling
629 Network, 1983-2009, Version: 2010-08-12, Path:
630 ftp://ftp.cmdl.noaa.gov/ccg/ch4/flask/event/, 2010.
631 Dlugokencky, E.J., P.M. Lang, A.M. Crotwell, K.A. Masarie, and M.J. Crotwell,
632 Atmospheric Methane Dry Air Mole Fractions from the NOAA ESRL Carbon Cycle.
633 Cooperative Global Air Sampling Network, 1983-2013, Version: 2014-06-24, 2014.

634 Drummond, J. R., Measurements of Pollution in the Troposphere (MOPITT), in The use of
635 EOS for Studies of Atmospheric Physics, edited by J. C. Gille and G. Visconti, pp. 77-101,
636 North Holland, Amsterdam, 1992
637 Duncan, B. N., Portman, D., Bey, I., and Spivakovsky, C. M.:Parameterization of OH for
638 efficient computation in chemical tracer models, J. Geophys. Res., 105 (D10), 12259–
639 12262, 2000.
640 Duncan, B. N., Martin, R. V., Staudt, A. C., Yevich, R. M., and Logan, J. A.: Interannual and
641 Seasonal Variability of Biomass Burning Emissions Constrained by Satellite Observations,
642 J. Geophys. Res., 108(D2), 4040, doi:10.1029/2002JD002378, 2003a.
643 Duncan, B.N., I. Bey, M. Chin, L.J. Mickley, T.D. Fairlie, R.V. Martin, and H. Matsueda,
644 Indonesian Wildfires of 1997: Impact on Tropospheric Chemistry, J. Geophys. Res., 108,
645 doi:10.1029/2002JD003195, 2003b.
646 Duncan, B. N., Logan, J. A., Bey, I., Megretskaia, I. A., Yantosca, R. M., Novelli, P. C.,
647 Jones, N. B., and Rinsland, C. P.: Global budget of CO, 1988–1997: Source estimates and
648 validation with a global model, J. Geophys. Res., 112(D22), D22301,
649 doi:10.1029/2007JD008459, 2007a.
650 Duncan, B. N., Strahan, S. E., Yoshida, Y., Steenrod, S. D., and Livesey, N.: Model study of
651 the cross-tropopause transport of biomass burning pollution, Atmos. Chem. Phys., 7,
652 3713–3736, doi:10.5194/acp-7-3713-2007, 2007b.
653 Duncan, B. and J. Logan, Model analysis of the factors regulating the trends and variability
654 of carbon monoxide between 1988 and 1997, Atmos. Chem. Phys., 8, 7389-7403, 2008.
655 Elshorbany, Y. F, Barnes, I., Becker, K. H, Kleffmann, J., and Wiesen, P.: Sources and
656 Cycling of Tropospheric Hydroxyl Radicals-An Overview, Zeitschrift für Physikalische
657 Chemie, 224, 967-987, DOI:10.1524/zpch.2010.6136, 2010b.
658 Elshorbany, Y. F., Kleffmann, J., Hofzumahaus, A., Kurtenbach, R., Wiesen, P., Dorn,H.-P.,
659 Schlosser, E., Brauers, T., Fuchs, H., Rohrer, F., Wahner, A., Kanaya, Y., Yoshino, A.,
660 Nishida, S., Kajii, Y., Martinez, M., Rudolf, M., Harder, H., Lelieveld, J., , Elste, T., Plass-
661 Dülmer, C., Stange, G., and Berresheim, H.: HOx Budgets during HOxComp: a Case
662 Study of HOx Chemistry under NOx limited Conditions, J. Geoophys. Res., 117, D03307,
663 doi: 10.1029/2011JD017008, 2012a.
664 Elshorbany, Y. F., Steil, B., Brühl, C., and Lelieveld, J.: Impact of HONO on global
665 atmospheric chemistry calculated with an empirical parameterization in the EMAC model,
666 Atmos. Chem. Phys., 12, 9977-10000, doi:10.5194/acp-12-9977-2012, 2012b.
667 Elshorbany, Y. F., Crutzen, P. J., Steil, B., Pozzer, A., Tost, H., and Lelieveld, J.: Global and
668 regional impacts of HONO on the chemical composition of clouds and aerosols, Atmos.
669 Chem. Phys., 14, 1167-1184, doi:10.5194/acp-14-1167-2014, 2014.
670 Fujino J, Nair R, Kainuma M, Masui T, Matsuoka Y, Multigas mitigation analysis on
671 stabilization scenarios using aim global model. The Energy Journal Special issue #3:343–
672 354, 2006.
673 Frankenberg, C., Aben, I., Bergamaschi, P., Dlugokencky, E. J., van Hees, R., Houweling,
674 S., et al. (2011). Global column-averaged methane mixing ratios from 2003 to 2009 as
675 derived from SCIAMACHY: Trends and variability, J. of Geophys. Res. doi:
676 10.1029/2010JD014849, 2011.

677 Ghosh, A., Patra, P. K., Ishijima, K., Umezawa, T., Ito, A., Etheridge, D. M., Sugawara, S.,
678 Kawamura, K., Miller, J. B., Dlugokencky, E. J., Krummel, P. B., Fraser, P. J.,
679 Steele, L. P., Langenfelds, R. L., Trudinger, C. M., White, J. W. C., Vaughn, B., Saeki, T.,
680 Aoki, S., and Nakazawa, T.: Variations in global methane sources and sinks during 1910–
681 2010, Atmos. Chem. Phys., 15, 2595-2612, doi:10.5194/acp-15-2595-2015, 2015.
682 Giglio, L., Randerson, J. T., van der Werf, G. R., Kasibhatla, P. S., Collatz, G. J., Morton, D.
683 C., and DeFries, R. S.: Assess- ing variability and long-term trends in burned area by
684 merging multiple satellite fire products, Biogeosciences, 7, 1171–1186, doi:10.5194/bg-7-
685 1171-2010, 2010.
686 Gloudemans, A. M. S., Schrijver, H., Hasekamp, O. P., and Aben, I.: Error analysis for CO
687 and CH4 total column retrievals from SCIAMACHY 2.3 μm spectra, Atmos. Chem. Phys.,
688 8, 3999-4017, doi:10.5194/acp-8-3999-2008, 2008.
689 Hijioka Y, Matsuoka Y, Nishimoto H, Masui T, Kainuma M.: Global GHG emission
690 scenarios under GHG concentration stabilization targets. J Glob Environ Eng 13:97–108,
691 2008.
692 Ho, S.-P., Edwards, D. P., Gille, J. C., Luo, M., Osterman, G. B., Kulawik, S. S., and
693 Worden, H.: A global comparison of carbon monoxide profiles and column amounts from
694 Tropospheric Emission Spectrometer (TES) and Measurements of Pollution in the
695 Troposphere (MOPITT), J. Geophys. Res., 114, D21307, doi:10.1029/2009JD012242,
696 2009.
697 Hodson, E., Poulter, B., Zimmermann, N. E.: The El Niño-Southern Oscillation and wetland
698 methane interannual variability, Geophys. Res. Lett., 38, L08810,
699 doi:10.1029/2011GL046861, 2011.
700 Holmes, C. D., Prather, M. J., Søvde, O. A., and Myhre, G.: Future methane, hydroxyl, and
701 their uncertainties: key climate and emission parameters for future predictions, Atmos.
702 Chem. Phys., 13, 285-302, doi:10.5194/acp-13-285-2013, 2013.
703 Houweling, S., Krol, M., Bergamaschi, P., Frankenberg, C., Dlugokencky, E. J., Morino, I.,
704 Notholt, J., Sherlock, V., Wunch, D., Beck, V., Gerbig, C., Chen, H., Kort, E. A.,
705 Röckmann, T., and Aben, I.: A multi-year methane inversion using SCIAMACHY,
706 accounting for systematic errors using TCCON measurements, Atmos. Chem. Phys., 14,
707 3991-4012, doi:10.5194/acp-14-3991-2014, 2014.
708 Khalil and Rasmussen (1984), The atmospheric lifetime of methylchloroform (CH4CCI3,)
709 Tellus, 368.3 17-332, 1984.
710 Kuze, A., Suto, H., Nakajima, M., and Hamazaki, T.: Thermal and near infrared sensor for
711 carbon observation Fourier-transform spectrometer on the Greenhouse Gases Observing
712 Satellite for greenhouse gases monitoring. Applied Optics, 48, 6716–6733, 2009.
713 Lamarque, J.-F., D.T. Shindell, B. Josse, P.J. Young, I. Cionni, V. Eyring, D. Bergmann, P.
714 Cameron-Smith, W.J. Collins, R. Doherty, S. Dalsoren, G. Faluvegi, G. Folberth, S.J.
715 Ghan, L.W. Horowitz, Y.H. Lee, I.A. MacKenzie, T. Nagashima, V. Naik, D. Plummer,
716 M. Righi, S. Rumbold, M. Schulz, R.B. Skeie, D.S. Stevenson, S. Strode, K. Sudo, S.
717 Szopa, A. Voulgarakis, and G. Zeng, 2013: The Atmospheric Chemistry and Climate
718 Model Intercomparison Project (ACCMIP): Overview and description of models,
719 simulations and climate diagnostics. *Geosci. Model Dev.*, **6**, 179-206, doi:10.5194/gmd-6-
720 179-2013.

721 Lelieveld, J., W. Peters, F. J. Dentener, and M. C. Krol, Stability of tropospheric hydroxyl
722 chemistry, J. Geophys. Res.,107(D23), 4715, doi:10.1029/2002JD002272, 2002.
723 Lin, S.-J.: A "vertically Lagrangian" finite-volume dynamical core for global models, Mon.
724 Weather Rev., 132(10), 2293–2307, doi:10.1175/1520-0493, 2004.
725 Luo, M., W. Read, S. Kulawik, J. Worden, N. Livesey, K. Bowman and R.Herman, Carbon
726 monoxide (CO) vertical profiles derived from joined TES and MLS measurements, J.
727 Geophys. Res. Atmos., 118, 10601–10613, doi:10.1002/jgrd.50800, 2013.
728 Myhre, G., Shindell, D., Bréon, F.-M., Collins, W., Fuglestvedt, J., Huang, J., Koch, D.,
729 Lamarque, J.-F., Lee, D., Mendoza, B., Nakajima, T., Robock, A., Stephens, G.,
730 Takemura, T. and Zhang, H.: Anthropogenic and Natural Radiative Forc- ing. In: *Climate*
731 *Change 2013: The Physical Science Basis. Contribution of Working Group I to the Fifth*
732 *Assessment Report of the Intergovernmental Panel on Climate Change* [Stocker, T.F., D.
733 Qin, G.-K. Plattner, M. Tignor, S.K. Allen, J. Boschung, A. Nauels, Y. Xia, V. Bex and
734 P.M. Midgley (eds.)]. Cambridge University Press, Cambridge, United Kingdom and New
735 York, NY, USA, 2013,
736 http://www.climatechange2013.org/images/report/WG1AR5_Chapter08_FINAL.pdf.
737 Manning M. R., Lowe, D. C., Moss, R. C., Bodeker, G. E., and Allan, W.: Short-term
738 variations in the oxidizing power of the atmosphere, Nature, 436, 18,
739 doi:10.1038/nature03900, 2005.
740 Molod, A., Takacs, L., Suarez, M., Bacmeister, J., Song, I.-S., and Eichmann, A.: The
741 GEOS-5 Atmospheric General Circulation Model: Mean Climate and Development from
742 MERRA to Fortuna, NASA/TM–2012-104606, Technical Report Series on Global
743 Modeling and Data Assimilation, Vol. 28, M. Suarez, Editor:
744 http://gmao.gsfc.nasa.gov/pubs/docs/tm28.pdf, 2012
745 Montzka, S. A., Krol, M., Dlugokencky, E., Hall, B., Joeckel, P., and Lelieveld, J.: Small
746 interannual variability of global atmospheric hydroxyl, Science, 331,
747 doi:10.1126/science.1197640, 2011.
748 Murray, L. T., Logan, J. A., and Jacob, D., J.:, Interannual variability in tropical tropospheric
749 ozone and OH: The role of lightning, J. Geophys. Res. Atmos., 118,
750 doi:10.1002/jgrd.50857, 2013.
751 Murray, L. T., Mickley, L. J., Kaplan, J. O., Sofen, E. D., Pfeiffer, M., and Alexander, B.:
752 Factors controlling variability in the oxidative capacity of the troposphere since the Last
753 Glacial Maximum, Atmos. Chem. Phys., 14, 3589-3622, doi:10.5194/acp-14-3589-2014,
754 2014.
755 Naik, V., Voulgarakis, A., Fiore, A. M., Horowitz, L. W., Lamarque, J.-F., Lin, M.,
756 Prather, M. J., Young, P. J., Bergmann, D., Cameron-Smith, P. J., Cionni, I.,
757 Collins, W. J., Dalsøren, S. B., Doherty, R., Eyring, V., Faluvegi, G., Folberth, G. A.,
758 Josse, B., Lee, Y. H., MacKenzie, I. A., Nagashima, T., van Noije, T. P. C.,
759 Plummer, D. A., Righi, M., Rumbold, S. T., Skeie, R., Shindell, D. T., Stevenson, D. S.,
760 Strode, S., Sudo, K., Szopa, S., and Zeng, G.: Preindustrial to present-day changes in
761 tropospheric hydroxyl radical and methane lifetime from the Atmospheric Chemistry and
762 Climate Model Intercomparison Project (ACCMIP), Atmos. Chem. Phys., 13, 5277-5298,
763 doi:10.5194/acp-13-5277-2013, 2013.

764 Novelli, P., Steele, P., Tans, P. P.: Mixing ratios of carbon monoxide in the troposphere, J.
765 Geophys. Res., 102, 12,855-12,861, doi: 10.1029/92JD02010, 1992.
766 Novelli, P., Masarie, K., A., Lang, P. M.: Distributions and recent changes in carbon
767 monoxide in the lower troposphere, J. Geosphys. Res., 103, 19,015-19,033, 1998.
768 Oman, L. D., J. R. Ziemke, A. R. Douglass, D. W. Waugh, C. Lang, J. M. Rodriguez, and J.
769 E. Nielsen (2011), The response of tropical tropospheric ozone to ENSO, Geophys. Res.
770 Lett., 38, L13706, doi:10.1029/2011GL047865, 2011.
771 Ott, L., Duncan, B., Pawson, S., Colarco, P., Chin, M., Randles, C., Diehl, T., and Nielsen,
772 E.: Influence of the 2006 Indonesian biomass burning aerosols on tropical dynamics
773 studied with the GEOS5 AGCM, J. Geophys. Res., 115, D14121,
774 doi:10.1029/2009JD013181, 2010.
775 Patra, P. K., Houweling, S., Krol, M., Bousquet, P., Belikov, D., Bergmann, D., Bian, H.,
776 Cameron-Smith, P., Chipperfield, M. P., Corbin, K., Fortems-Cheiney, A., Fraser, A.,
777 Gloor, E., Hess, P., Ito, A., Kawa, S. R., Law, R. M., Loh, Z., Maksyutov, S., Meng, L.,
778 Palmer, P. I., Prinn, R. G., Rigby, M., Saito, R., and Wilson, C.: TransCom model
779 simulations of CH4 and related species: linking transport, surface flux and chemical loss
780 with CH4 variability in the troposphere and lower stratosphere, Atmos. Chem. Phys., 11,
781 12813-12837, doi:10.5194/acp-11-12813-2011, 2011.
782 Pawson, S., R. S. Stolarski, Douglass, A. R. , Newman, P. A. , Nielsen, J. E., Frith, S. M.,
783 and Gupta, M. L.: Goddard Earth Observing System chemistry-climate model simulations
784 of stratospheric ozone-temperature coupling between 1950 and 2005, J. Geophys. Res.,
785 113, D12103, doi:10.1029/2007JD009511, 2008.
786 Prather, M.: Lifetimes and Eigen states in atmospheric chemistry, Geophys. Res. Lett., 21, 9,
787 801-4, 1994.
788 Prather, M.: Time scales in atmospheric chemistry: Theory, GWPs for CH4 and CO, and
789 runaway growth, Geophys. Res. Lett., 23, 19, 2597–2600, DOI: 10.1029/96GL02371,
790 1996.
791 Prather, M. J., C. D. Holmes, and J. Hsu.: Reactive greenhouse gas scenarios: Systematic
792 exploration of uncertainties and the role of atmospheric chemistry, Geophys. Res. Lett.,
793 39, L09803, doi:10.1029/2012GL051440, 2012.
794 Prinn, R. G., Huang, J., Weiss, R. F., Cunnold, D. M., Fraser, P. J., Simmonds, P. G.,
795 McCulloch, A., Harth, C., Reimann, S., Salameh, P., O'Doherty, S., Wang, R. H. J.,
796 Porter, L. W., Miller, B. R., and Krummel, P. B.: Evidence for variability of atmospheric
797 hydroxyl radicals over the past quarter century, Geophys. Res. Lett., 32, L07809,
798 doi:10.1029/2004GL022228, 2005.
799 Randerson, J.T., G.R. van der Werf, L. Giglio, G.J. Collatz, and P.S. Kasibhatla.. Global Fire
800 Emissions Database, Version 3 (GFEDv3.1). Data set. Available on-line
801 [http://daac.ornl.gov/] from Oak Ridge National Laboratory Distributed Active Archive
802 Center, Oak Ridge, Tennessee, USA. doi:10.3334/ORNLDAAC/1191, 2013.
803 Rienecker, M., et al., The GEOS-5 data assimilation system – Documentation of Versions
804 5.0.1, 5.1.0, and 5.2.0, Technical Report Series on Global Modeling and Data
805 Assimilation, Vol. 27, http://gmao.gsfc.nasa.gov/pubs/docs/GEOS5_104606-Vol27.pdf,
806 2008.

807 Rigby, M., et al., Renewed growth of atmospheric methane, Geophys. Res. Lett., 35,
808 L22805, doi:10.1029/2008GL036037, 2008.
809 Rohrer, F., and H. Berresheim, Strong correlations between levels of tropospheric hydroxyl
810 radicals and solar ultraviolet radiation, Nature, 442, doi:10.1038/nature04924, 2006.
811 Franz Rohrer, Keding Lu, Andreas Hofzumahaus, Birger Bohn, Theo Brauers, Chih-Chung
812 Chang, Hendrik Fuchs, Rolf Häseler, Frank Holland, Min Hu, Kazuyuki Kita, Yutaka
813 Kondo, Xin Li, Shengrong Lou, Andreas Oebel, Min Shao, Limin Zeng, Tong Zhu,
814 Yuanhang Zhang & Andreas Wahner, Maximum efficiency in the hydroxyl-radical-based
815 self-cleansing of the troposphere, Nature Geoscience 7, 559–563, doi:10.1038/ngeo2199,
816 2014.
817 Saito, R., Patra, P. K., Deutscher, N., Wunch, D., Ishijima, K., Sherlock, V.,
818 Blumenstock, T., Dohe, S., Griffith, D., Hase, F., Heikkinen, P., Kyrö, E., Macatangay, R.,
819 Mendonca, J., Messerschmidt, J., Morino, I., Notholt, J., Rettinger, M., Strong, K.,
820 Sussmann, R., and Warneke, T.: Technical Note: Latitude-time variations of atmospheric
821 column-average dry air mole fractions of CO2, CH4 and N2O, Atmos. Chem. Phys., 12,
822 7767-7777, doi:10.5194/acp-12-7767-2012, 2012.
823 Saito, R., Patra, P. K., Sweeney, C., Machida, T., Krol, M., Houweling, S., Bousquet, P.,
824 Agusti-Panareda, A., Belikov, D., Bergmann, D., Bian, H., Cameron-Smith, P., P.
825 Chipperfield, M., Fortems-Cheiney, A., Fraser, A., V. Gatti, L., Gloor, E., Hess, P., R.
826 Kawa, S., M. Law, R., Locatelli, R., Loh, Z., Maksyutov, S., Meng, L., B. Miller, J., I.
827 Palmer, P., G. Prinn, R., Rigby, M., and Wilson, C.: TransCom model simulations of
828 methane: Comparison of vertical profiles with aircraft measurements, J. Geophys. Res.
829 Atmos., 118,3891–3904,doi:10.1002/jgrd.50380, 2013.
830 Schneising, O., et al., Three years of greenhouse gas column-averaged dry air mole fractions
831 retrieved from satellite – Part 2: Methane, Atmos. Chem. Phys., 9, 443-465. Schneising,
832 O., et al. (2011), Long-term analysis of carbon dioxide and methane column- averaged
833 mole fractions retrieved from SCIAMACHY, Atmos. Chem. Phys., 11, 2863-2880.
834 Shindell, D. T., Faluvegi, G., Stevenson, D. S., Krol, M. C., Emmons, L. K., Lamarque, J.-F.,
835 P´etron, G., Dentener, F. J., Ellingsne, K., Schultz, M. G., Wild, O., Amann, M., Atherton,
836 C. S., Bergmann, D. J., Bey, I., Butler, T., Cofala, J., Collins, W. J., Derwent, R. G.,
837 Doherty, R. M., Drevet, J., Eskes, H. J., Fiore, A. M., Gauss, M., Hauglustaine, D. A.,
838 Horowitz, L.W., Isaksen, I. S. A., Lawrence, M. G., Montanaro, V., M¨uller, J.-F., Pitari,
839 G., Prather, M. J., Pyle, J. A., Rast, S., Rodriguez, J. M., Sanderson, M. G., Savage, N. H.,
840 Strahan, S. E., Sudo, K., Szopa, S., Unger, N., van Noije, T. P. C., and Zeng, G.:
841 Multimodel simulations of carbon monoxide: Comparison with observations and projected
842 near-future changes, J. Geophys. Res., 111, D19306, doi:10.1029/2006JD007100, 2006.
843 Shindell, D., et al., Improved attribution of climate forcing to emissions, Science, 326,
844 October 2009. Spivakovsky, C., et al. (2000), Three - dimensional climatological
845 distribution of tropospheric OH: Update and evaluation, J. Geophys. Res., 105(D7), 8931-
846 8980. 2009.
847 Schneising, O., Buchwitz, M., Burrows, J. P., Bovensmann, H., Bergamaschi, P., and Peters,
848 W., Three years of greenhouse gas column-averaged dry air mole fractions retrieved from
849 satellite - Part 2: Methane, Atmos. Chem. Phys., 9, 443-465, 2009.

Schneising, O., Buchwitz, M., Reuter, M., Heymann, J., Bovensmann, H., and Burrows, J. P.: Long-term analysis of carbon dioxide and methane column-averaged mole fractions retrieved from SCIAMACHY, Atmos. Chem. Phys., 11, 2863-2880, doi:10.5194/acp-11-2863-2011, 2011.

Schultz, M., S. Rast, M. van het Bolscher, T. Pulles, R. Brand, J. Pereira, B. Mota, A. Spessa, S. Dalsøren, T. van Nojie, S. Szopa, Emission data sets and methodologies for estimating emissions, RETRO project report D1-6, Hamburg, 26 Feb 2007 (http://gcmd.gsfc.nasa.gov/records/GCMD_GEIA_RETRO.html).

Spivakovsky, C M., Logan, J A., Montzka, S A., Balkanski, Y J. Foreman-Fowler, M., Jones, D B A., Horowitz, L W., Fusco, A C., Brenninkmeijer, C A M., Prather, M J., Wofsy, S C., and McElroy, M B.: Three-dimensional climatological distribution of tropospheric OH: Update and evaluation, J. Geophys. Res., 105, D7, 8931–8980, doi:10.1029/1999JD901006, 2000.

Stauffer, B., et al., Methane concentration in the glacial atmosphere was only half that of the preindustrial Holocene, Nature 332, 812 - 814 (28 April 1988); doi:10.1038/332812a0, 1988.

Stone, D., L.K. Whalley, D.E. Heard.: Tropospheric OH and HO_2 radicals: field measurements and model comparisons. Chemical Society Reviews, 41:19, 6348, DOI:10.1039/c2cs35140d, 2012.

Strahan, S.E., B.N. Duncan and P. Hoor, Observationally-derived diagnostics of transport in the lowermost stratosphere and their application to the GMI chemistry transport model, Atmos. Chem. Phys., 7, 2435-2445, 2007.

van Vuuren DP, Edmonds J, Kainuma M, Riahi K, Thomson A, Hibbard K, Hurtt GC, Kram T, Krey V, Lamarque JF, Masui T, Meinshausen M, Nakicenovic N, Smith SJ, Rose SK.: The representative concentration pathways: an overview. Climate Change 109, 5–31, 2011.

Voulgarakis, A., M. E. Marlier, G. Faluvegi, D. T. Shindell, K. Tsigaridis, and S. Mangeon, Interannual variability of tropospheric trace gases and aerosols: The role of biomass burning emissions, J. Geophys. Res. Atmos., 120, doi:10.1002/2014JD022926,2015.

Wang, J., et al., A 3-D model analysis of the slowdown and interannual variability in the methane growth rate from 1988 to 1997, Global Biogeochemical Cycles, 18, GB3011, doi:10.1029/2003GB002180, 2004.

Wainwright, C. D., Pierce, J. R., Liggio, J., Strawbridge, K. B., Macdonald, A. M., and Leaitch, R. W.: The effect of model spatial resolution on Secondary Organic Aerosol predictions: a case study at Whistler, BC, Canada, Atmos. Chem. Phys., 12, 10911-10923, doi:10.5194/acp-12-10911-2012, 2012.

Wehner, M. F., K. A. Reed, F. Li, Prabhat, J. Bacmeister, C.-T. Chen, C. Paciorek, P. J. Gleckler, K. R. Sperber, W. D. Collins, A. Gettelman, and C. Jablonowski (2014), The effect of horizontal resolution on simulation quality in the Community Atmospheric Model, CAM5.1, J. Adv. Model. Earth Syst., 6, 980–997, doi:10.1002/2013MS000276.

Wild, O., and Palmer, P. I.: How sensitive is tropospheric oxidation to anthropogenic emissions?, Geophys. Res. Lett., 35, L22802, doi:10.1029/2008GL035718, 2008.

892 Wolter, K., and M. S. Timlin, El Niño/Southern Oscillation behaviour since 1871 as
893 diagnosed in an extended multivariate ENSO index (MEI.ext). Intl. J. Climatology, 31,
894 1074-1087, DOI: 10.1002/joc.2336, 2011.
895 Worden, H. M., Deeter, M. N., Edwards, D. P., Gille, J. C., Drummond, J. R., and Nédélec,
896 P.: Observations of near-surface carbon monoxide from space using MOPITT
897 multispectral retrievals, J. Geophys., Res., 115, D18314, doi:10.1029/2010JD014242,
898 2010.
899 Ziemke, J. R., Douglass, A. R., Oman, L. D., Strahan, S. E., and Duncan, B. N.:
900 Tropospheric ozone variability in the tropics from ENSO to MJO and shorter timescales,
901 Atmos. Chem. Phys., 15, 8037-8049, doi:10.5194/acp-15-8037-2015, 2015.
902

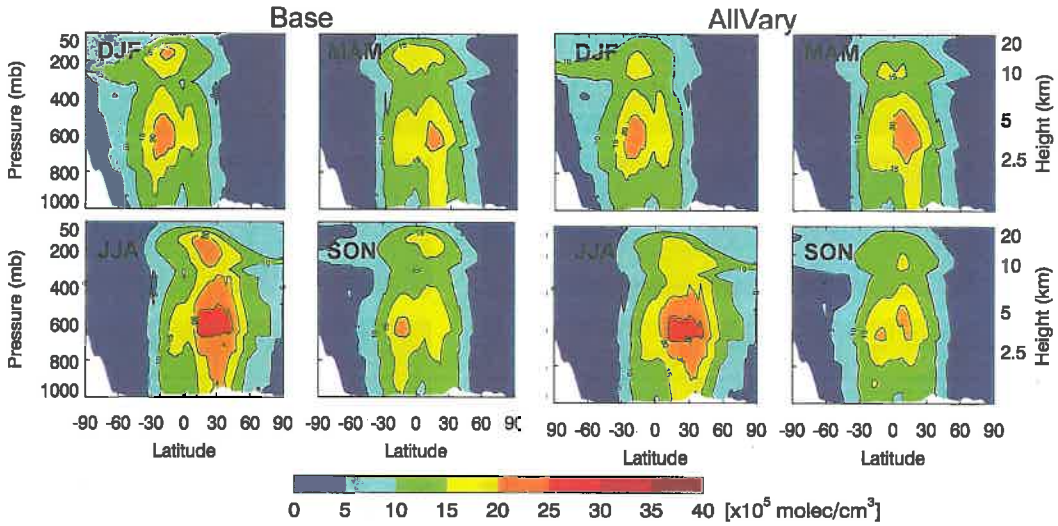

Figure 1: Seasonal zonal mean of OH ($x10^5$molecules/cm^3) averaged over the simulation period (1988-2007) for the *Base* (left 4 panels) and the *AllVary* (right 4 panels) scenarios for December-February (DJF), March-May (MAM), June-August (JJA) and September-November (SON).

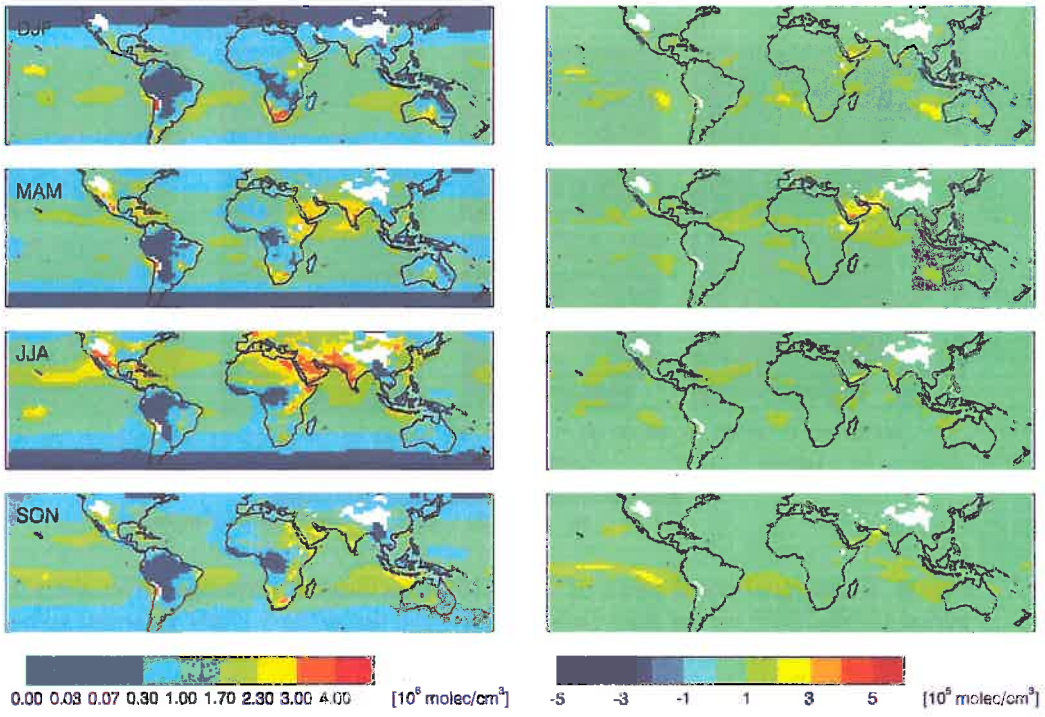

Figure 2: Seasonal mean OH (left column) from 1988 to 2007 for the *Base* scenario and their corresponding standard deviation (right column) at 850 mbar. Note the different color scales.

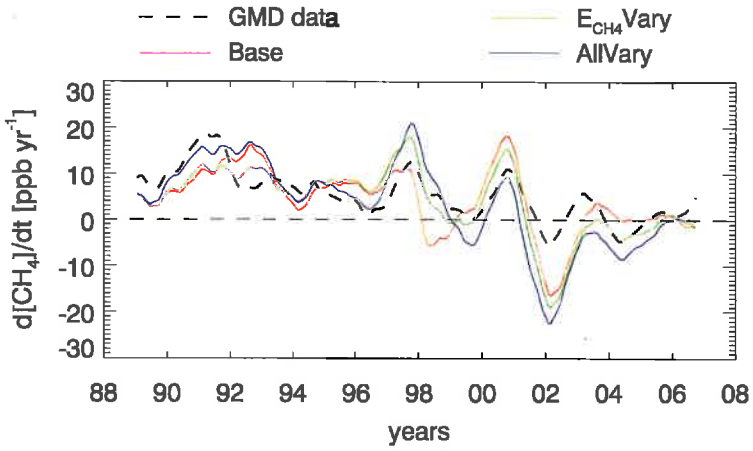

Figure 3: Global growth rate of simulated methane by different scenarios as compared to the growth rate from GMD measurements (all available stations).

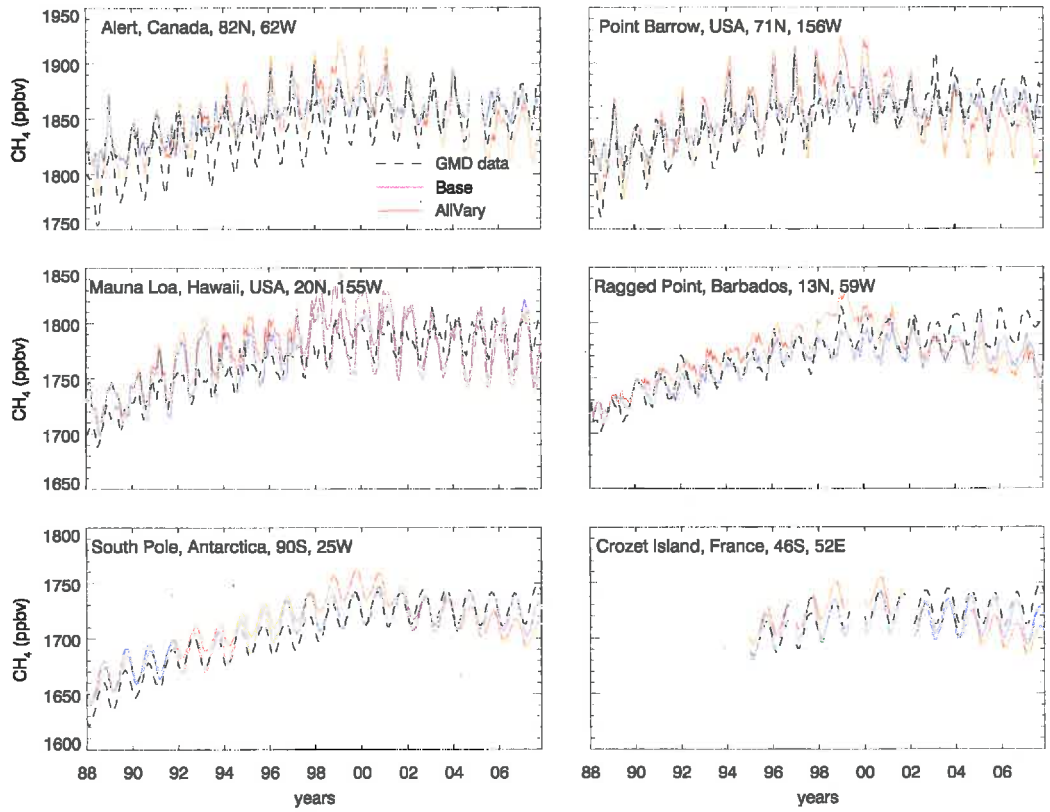

Figure 4: Monthly mean simulated near surface METHANE levels from the *Base* and *AllVary* scenarios as compared to those measured at GMD stations. Similar figures for the other scenarios are shown in the supplementary materials.

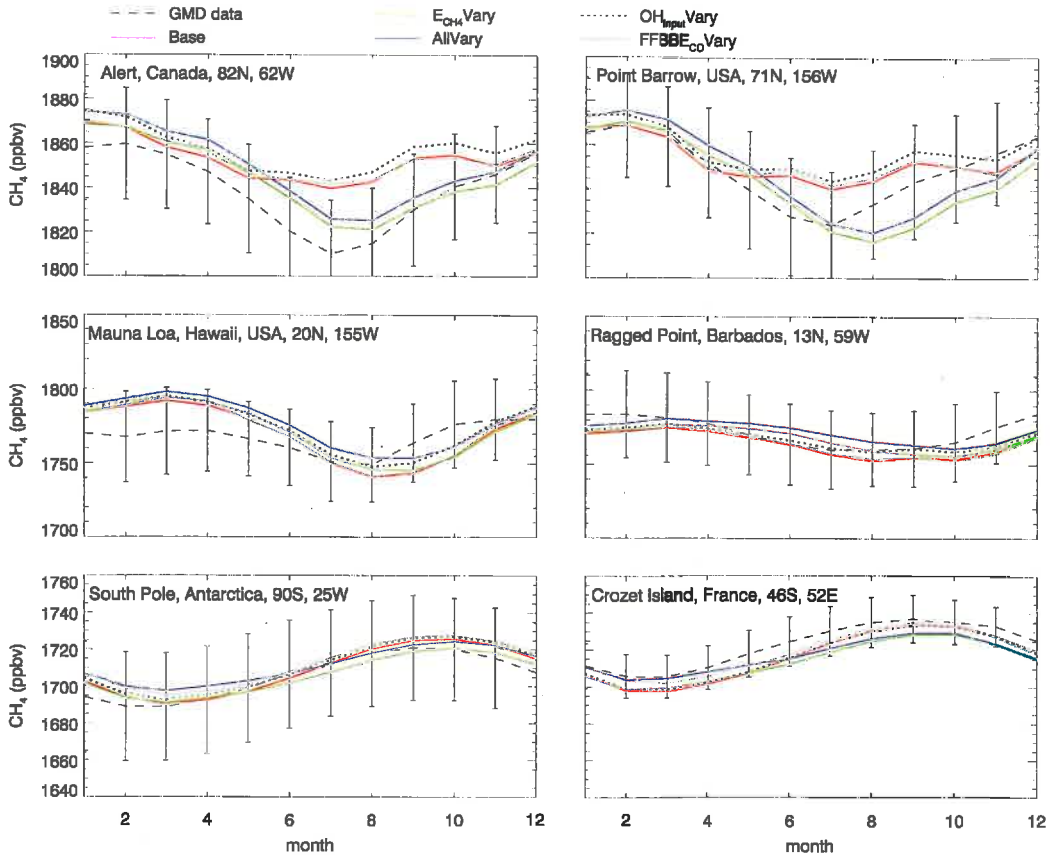

Figure 5: Seasonal mean measured and simulated near surface METHANE over the entire simulation period by different scenarios.

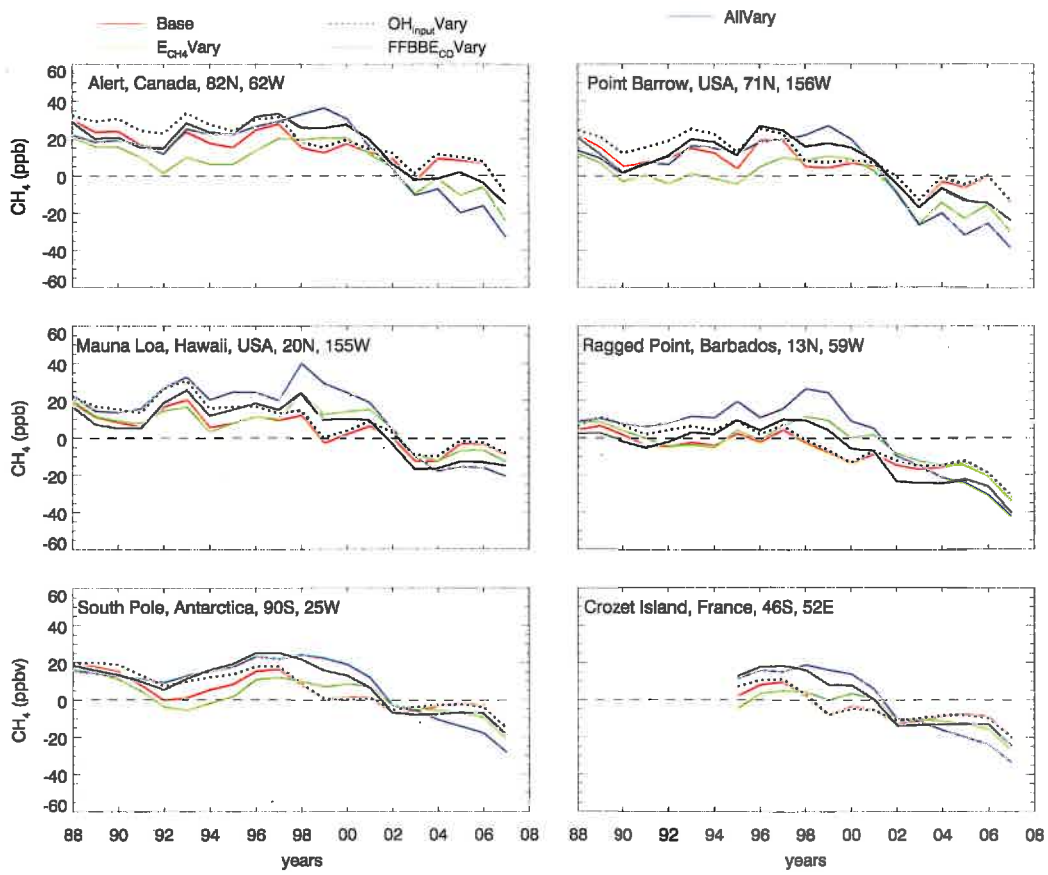

Figure 6: Difference (simulated-measured) of near surface METHANE mixing ratios simulated for different scenarios.

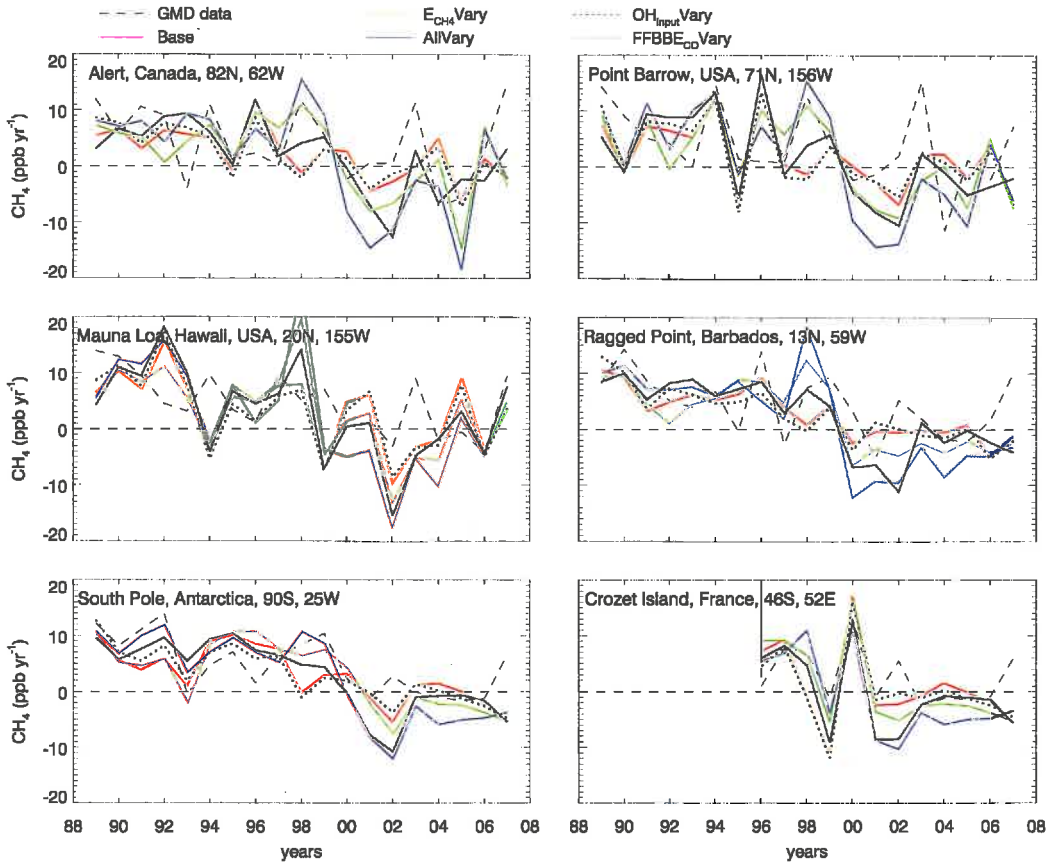

Figure 7: Growth rates of measured and simulated near surface methane by different scenarios. Similar figures for the other scenarios and GMD stations are in the supplementary materials.

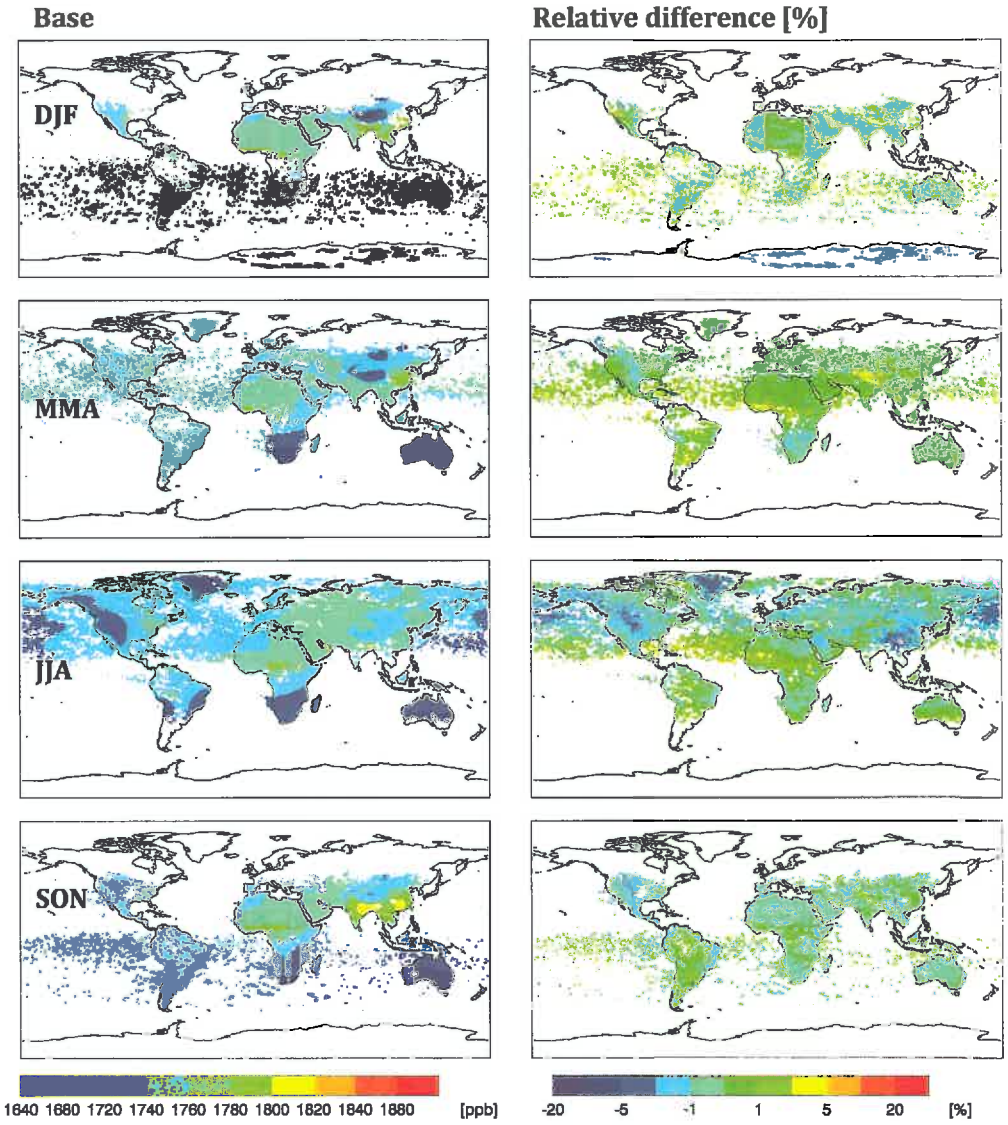

Figure 8: Seasonal mean simulated (*Base* scenario) methane dry column (ppbv, left panel) and the relative difference (%, Base-SCIAMACHY/SCIAMACHY, right panel) for 2004. Simulated methane levels are sampled and gridded to SCIAMACHY data.

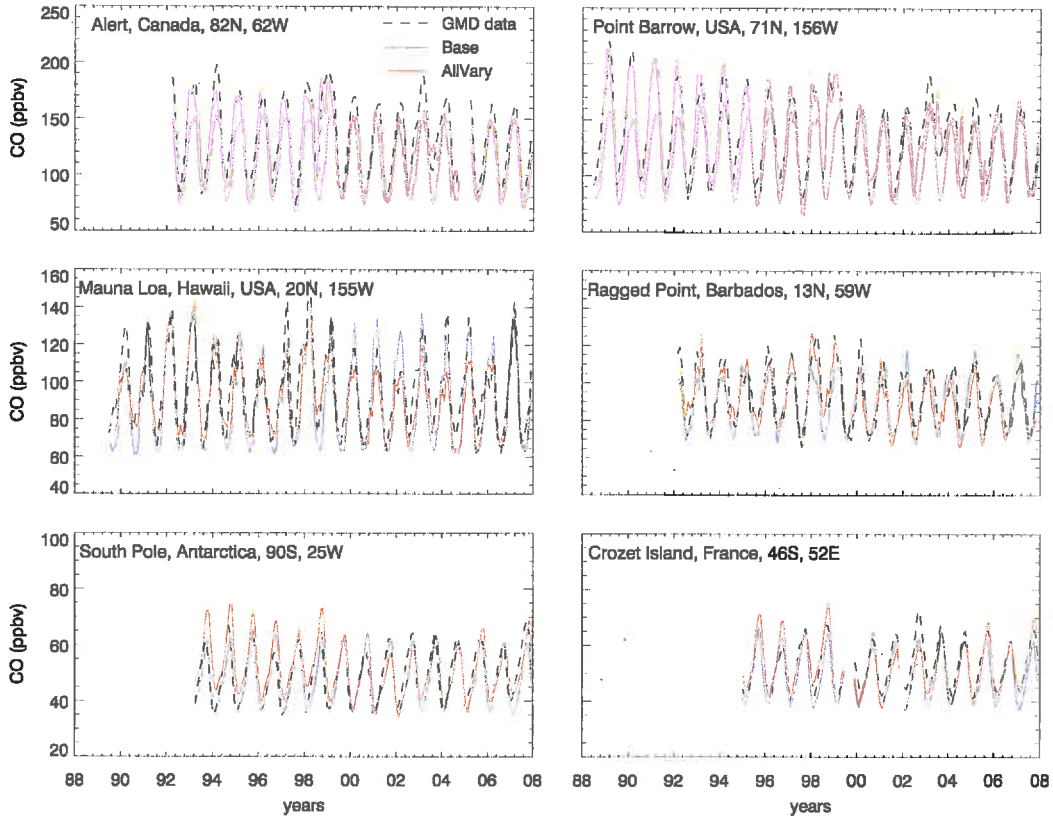

Figure 9: Measured and simulated monthly near surface CO levels of the Base and AllVary scenarios. Similar figures for the other scenarios are in the supplementary materials.

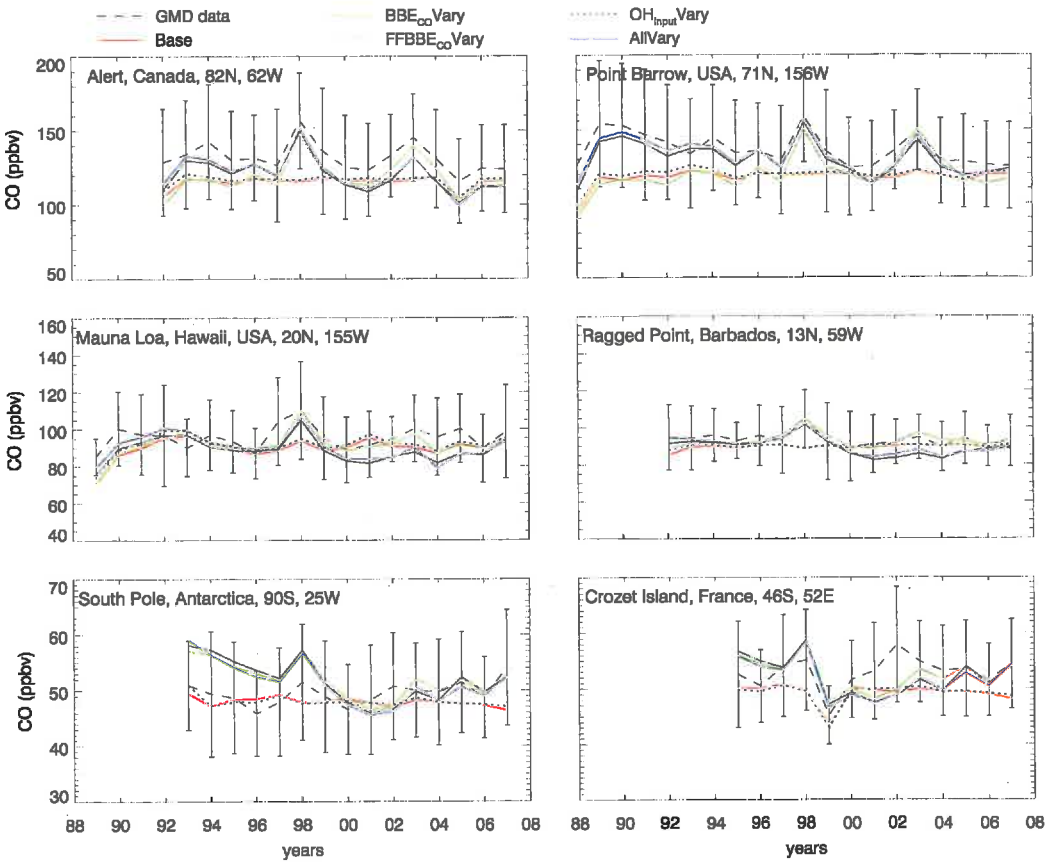

Figure 10: Annual mean measured and simulated near surface CO levels by different scenarios.

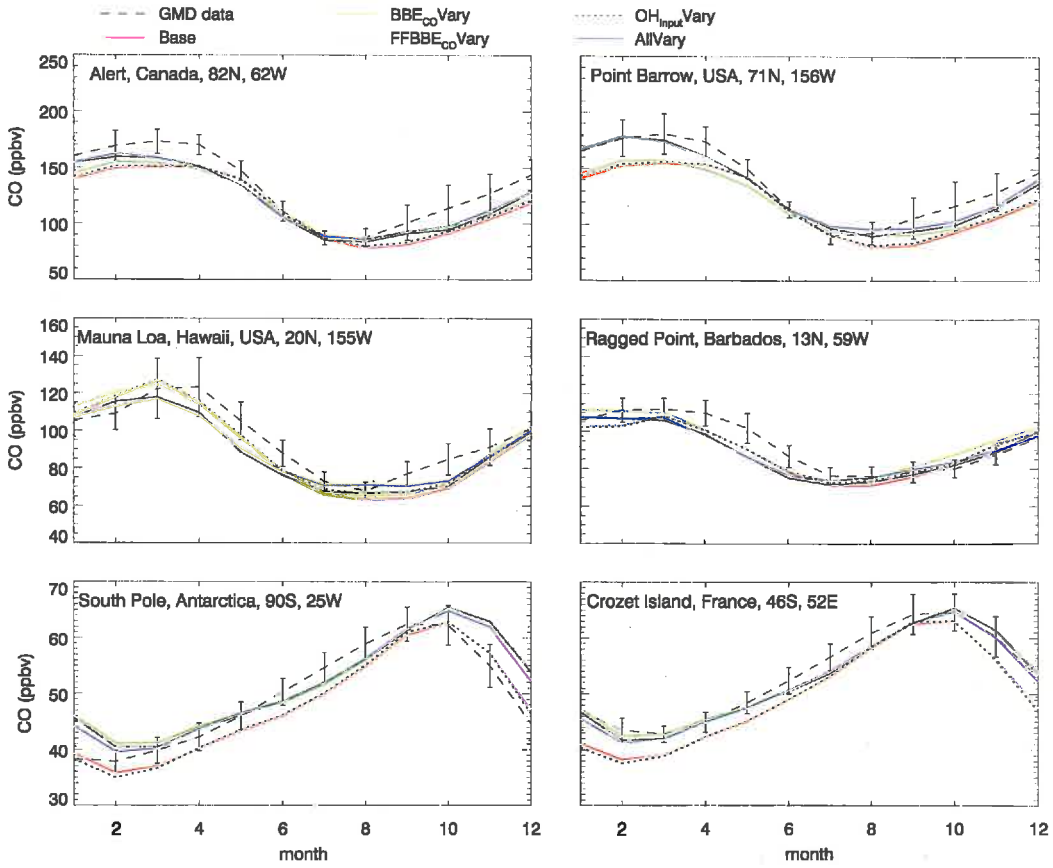

Figure 11: Seasonal mean (1988- 2007) measured and simulated near surface CO mixing ratios for different scenarios.

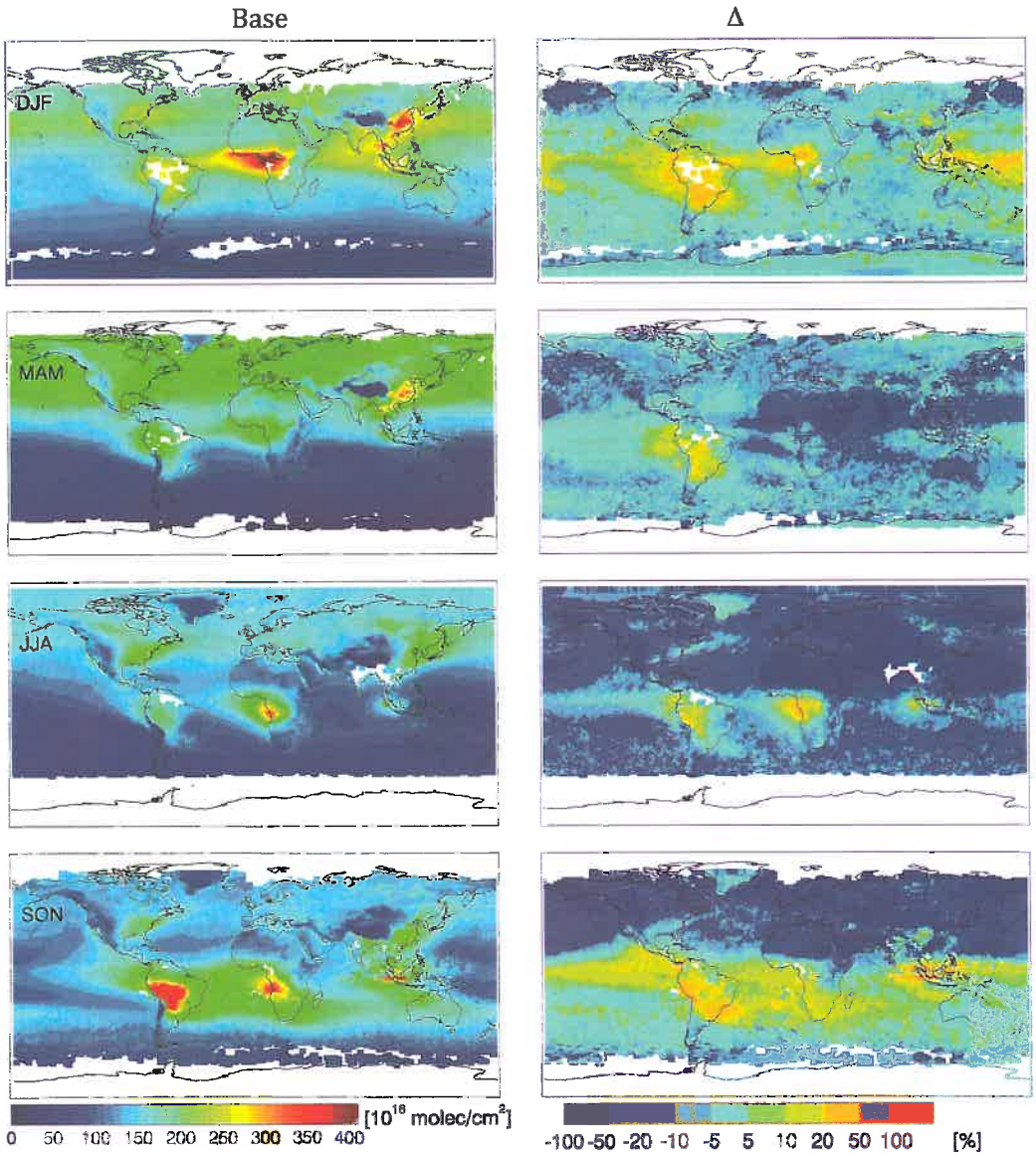

Figure 12: Seasonal mean (2006-2007) simulated (Base, left column) and relative difference (Base-MOPITT/MOPITT, right column) of the CO columns as compared to the MOPITT data. The 2006-2007 period was selected to be comparable for that of the TES_MLS.

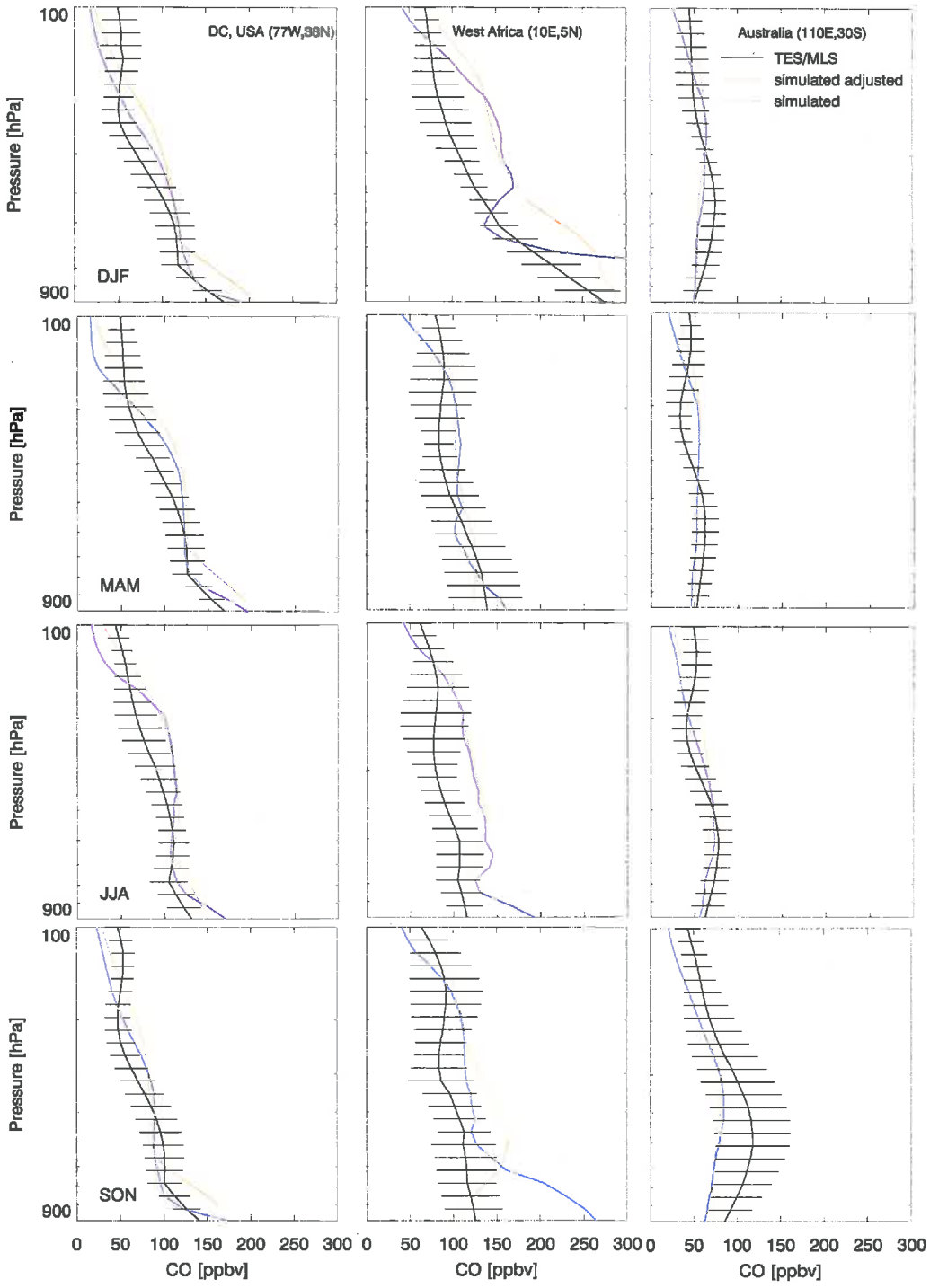

Figure 13: Seasonal mean (2006-2007) vertical profiles of CO from TES/MLS data, the Base scenario ('simulated') and simulated and adjusted with the averaging kernel (labeled as 'simulated adjusted') CO over selected locations using the *Base* scenario. The error bars indicate the mean standard deviation of TES/MLS CO joint product.

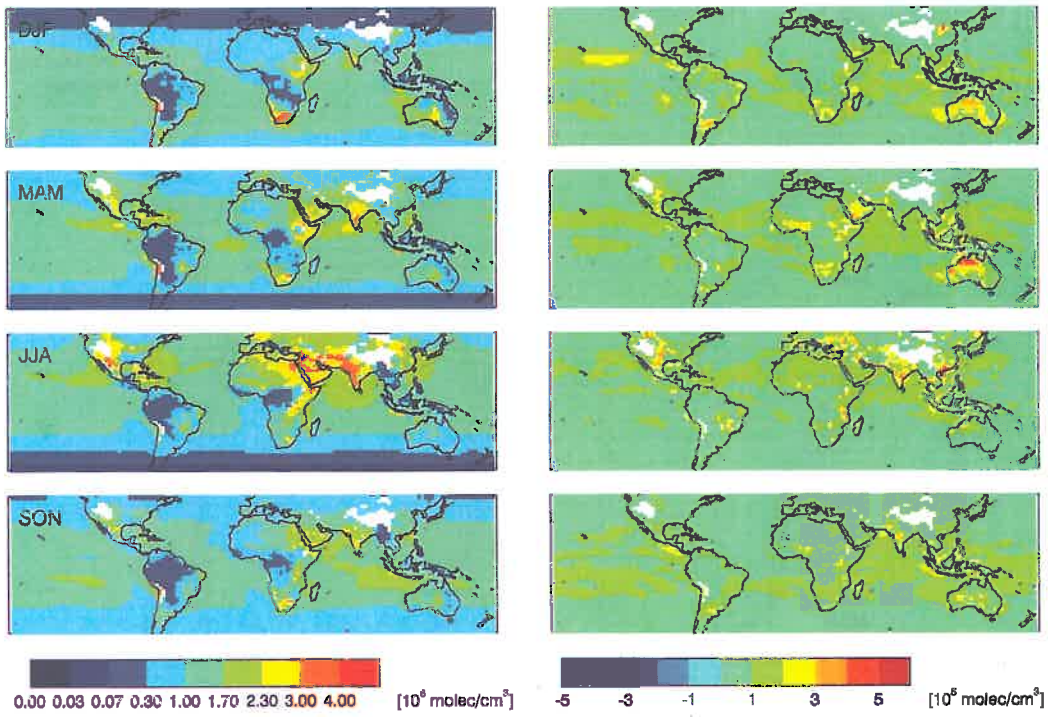

Figure 14: Seasonal mean OH (left column, 10^6 molecules/cm^3) from 1988-2007 for the AllVary scenario with standard deviation (right column, 10^5 molecules/cm^3) at 850 mbar.

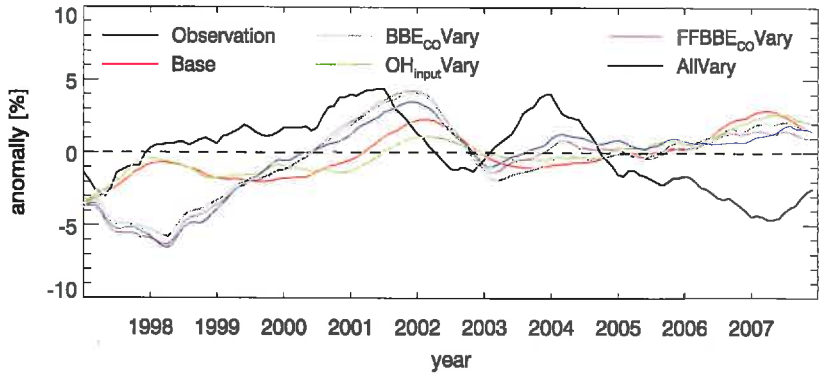

Figure 15: Anomalies of the global mass weighted pseudo first order rate constant of OH reaction with MCF, for both measured (black, adopted from Montzka et al., 2011) and simulated by different scenarios.

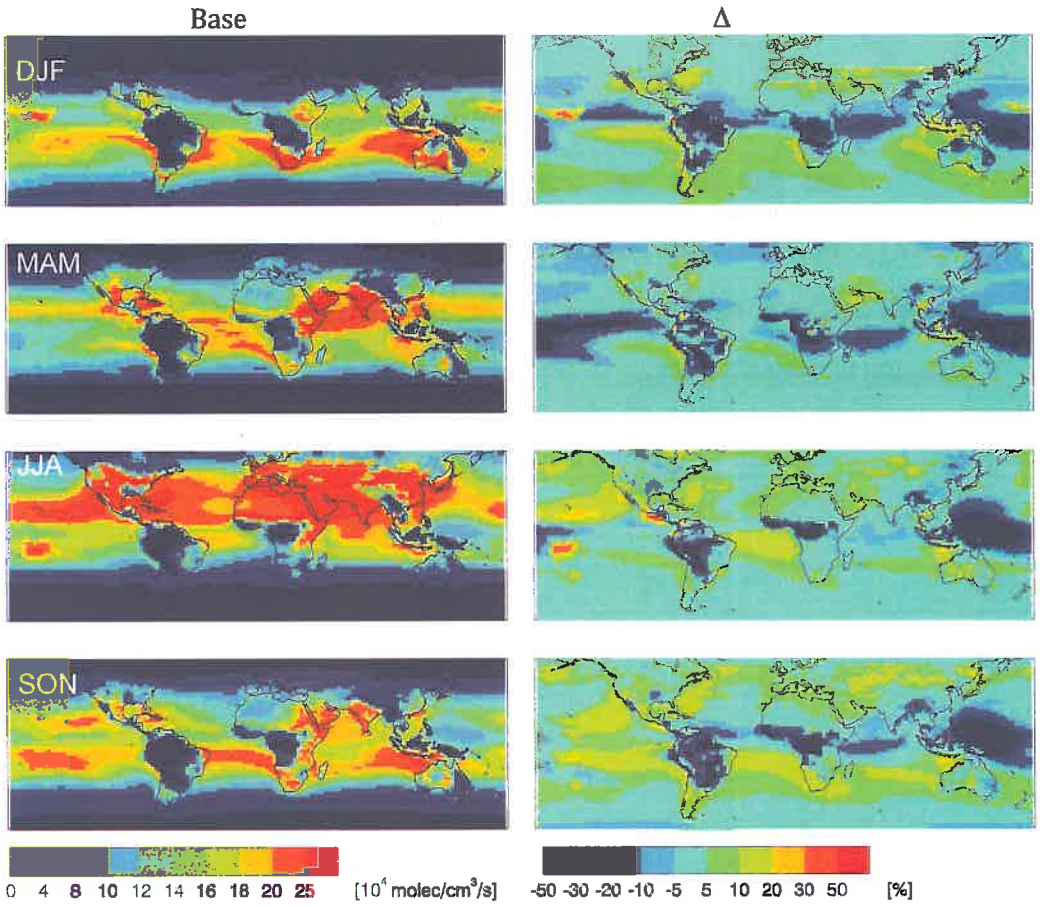

Figure 16: Seasonal mean (1988-2007) of tropospheric methane loss rate (left column) with relative difference compared to the AllVary scenario (Base-AllVary/Base, right column).

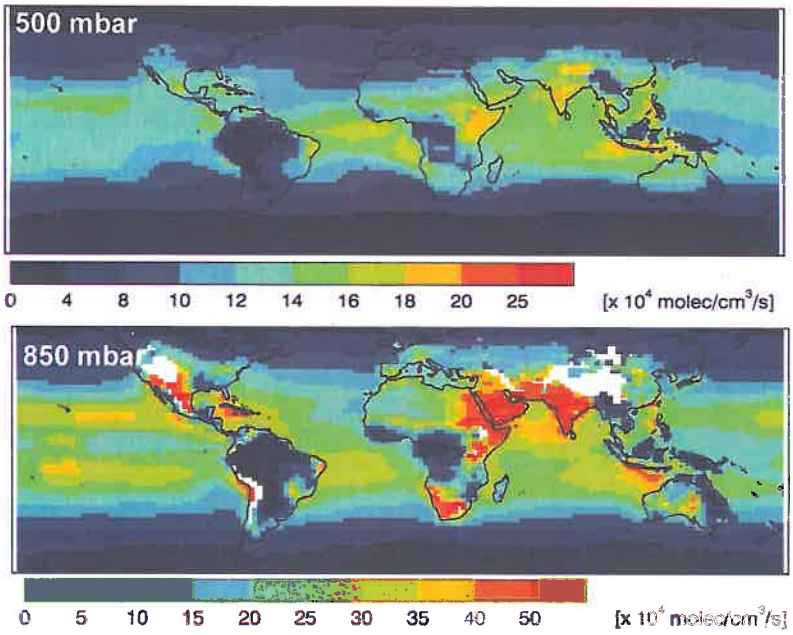

Figure 17: Mean methane loss rate (1988-2007) at 500 mb (top) and 850 mb (bottom) for the Base scenario.

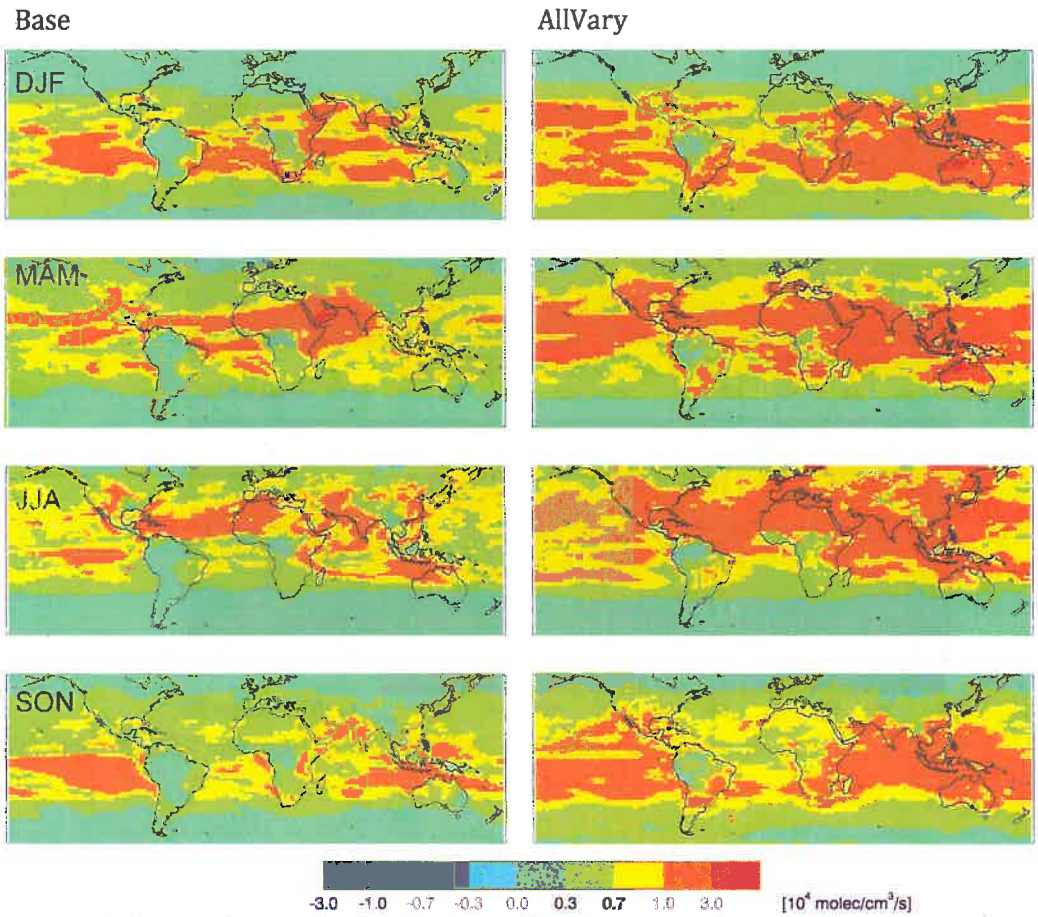

Figure 18: Seasonal mean (1988-2007) standard deviation of tropospheric methane loss rate from the Base (left column) and AllVary (right column) scenarios.

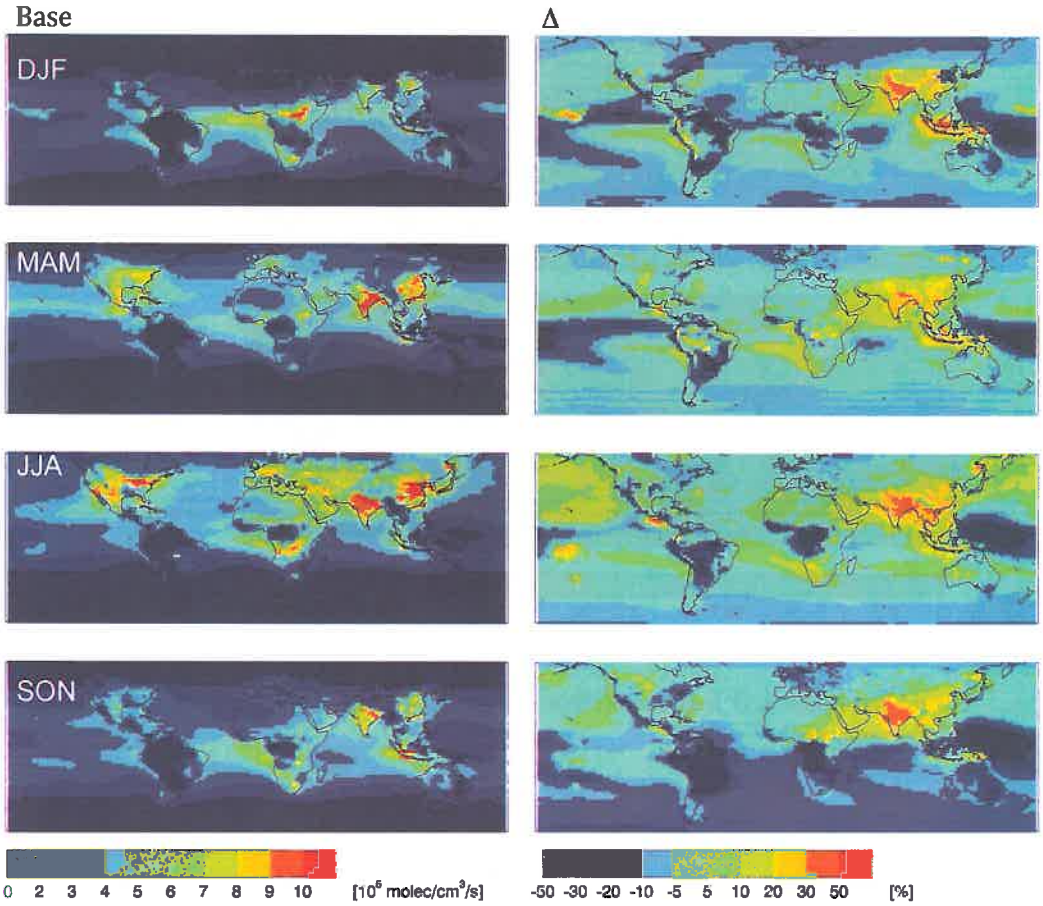

Figure 19: Seasonal mean (1988-2007) tropospheric CO loss rate (left column) with relative difference compared to the AllVary Scenario (Base-AllVary/Base, right column).

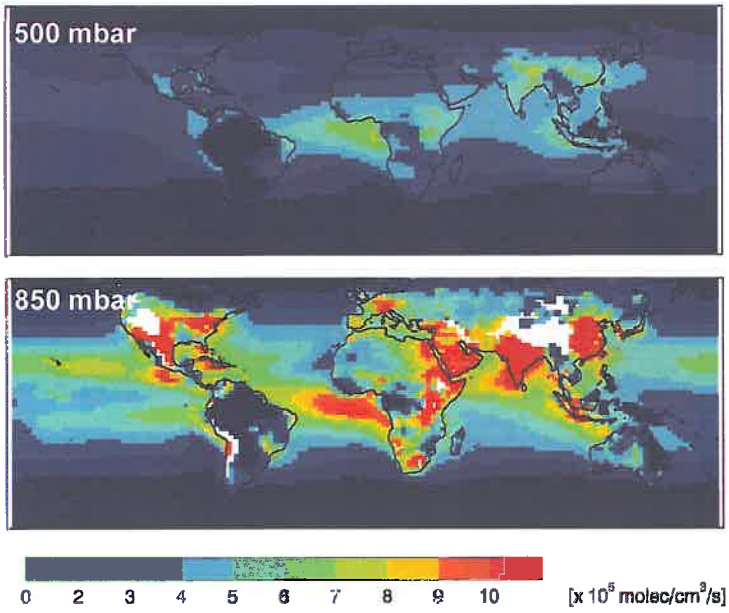

Figure 20: Mean CO loss rate (1988-2007) at 500 mb (top) and 850 mb (bottom) for the Base scenario.

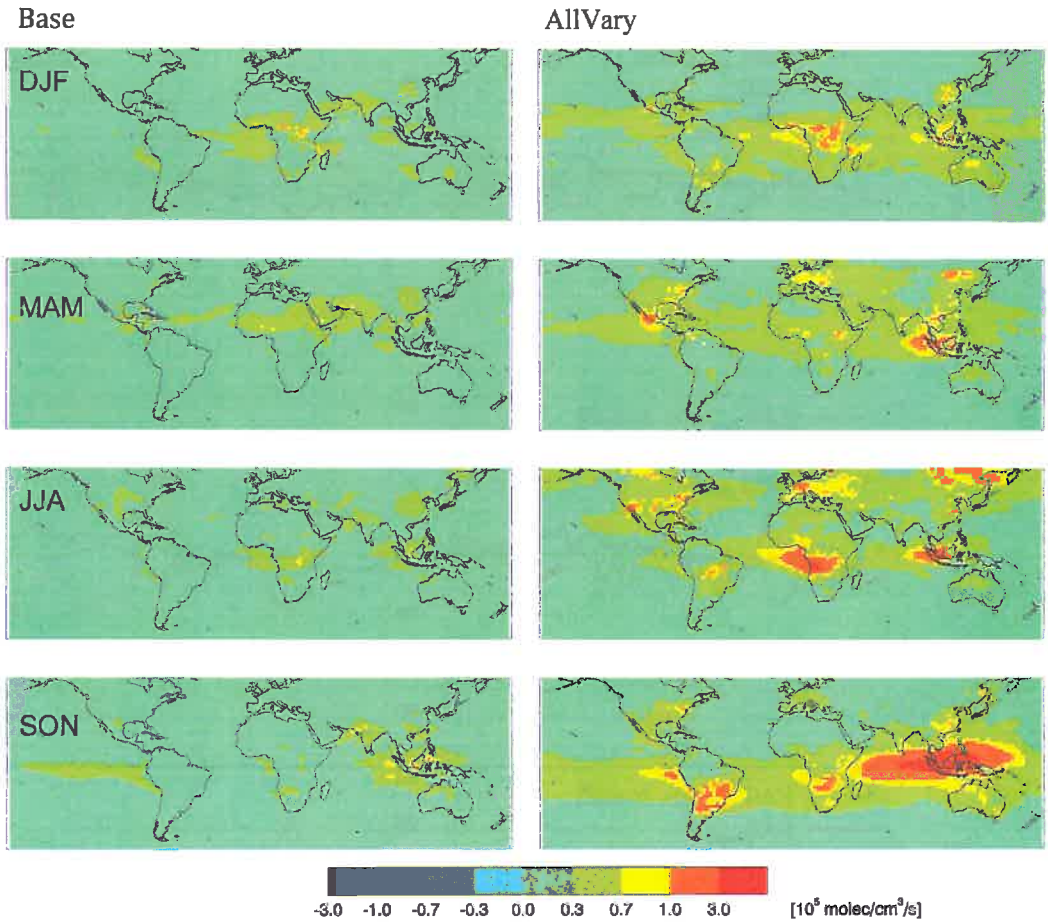

Figure 21: Seasonal mean (1988-2007) standard deviation of the tropospheric CO loss rate from the Base (left column) and AllVary (right column) scenarios.

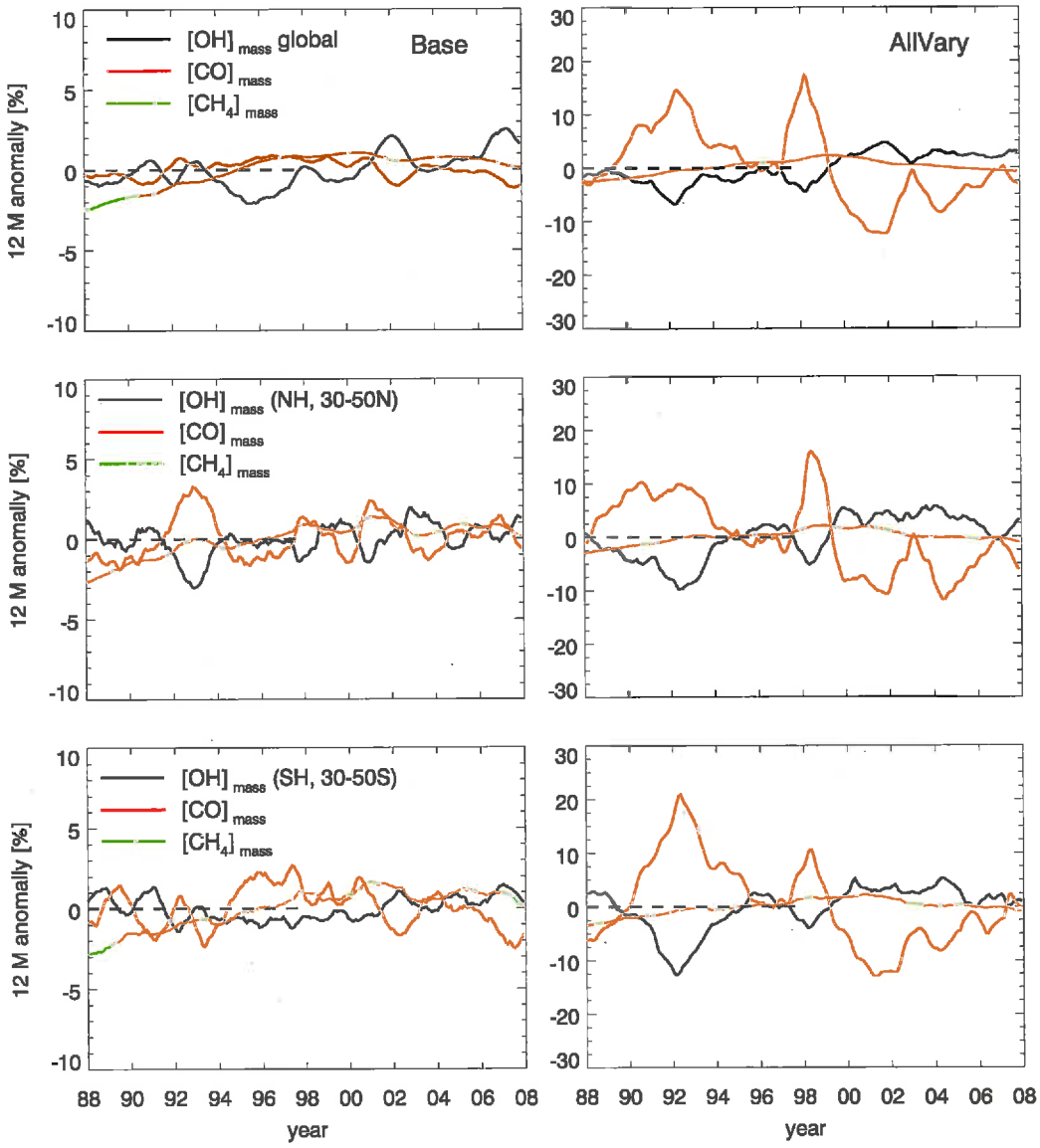

Figure 22: Simulated anomalies of the mass-weighted OH, CO and methane (12 month running mean), integrated globally, over the northern hemisphere, southern hemisphere from the Base (left) and the AllVary (right) scenarios. Note the different scales on the y-axes.

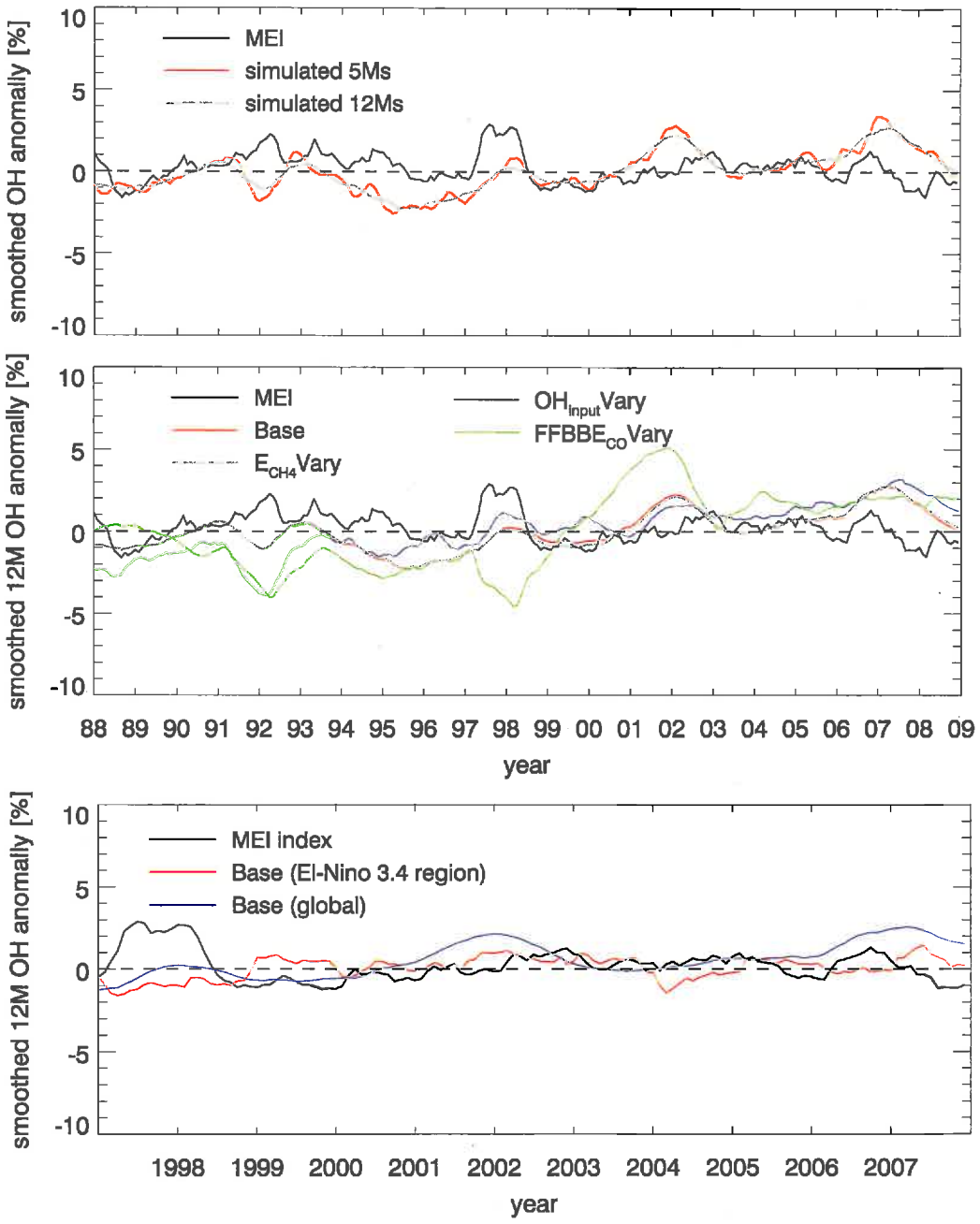

Figure 23: Upper panel: Anomalies of the global mass weighted OH compared to the Multivarient ENSO Index (MEI, black line). Black and gray lines are 12-month running mean while the red line is 5-month running mean. Middle panel: 12 month running mean of MEI and simulated mass weighted OH anomaly from different scenarios. Lower panel: 12 month running mean of MEI and simulated mass weighted OH anomaly integrated both globally and over the El-Nino 3.4 region.